Università Cattolica del Sacro Cuore
Dipartimento di Matematica e Fisica

Dynamics of Non-Equilibrium States in Solids Induced by Ultrashort Coherent Pulses

Ph.D. Thesis

Claudio Giannetti
Brescia, 2004

Corso di Dottorato in Fisica, Astrofisica e Fisica Applicata,
XVII° ciclo
Università degli Studi di Milano, Facoltà di Scienze Matematiche, Fisiche e Naturali,
Dipartimento di Fisica, Milano (Italy)
Università Cattolica del Sacro Cuore, Facoltà di Scienze Matematiche, Fisiche e Naturali,
Dipartimento di Matematica e Fisica, Brescia (Italy) (Sede Consorziata)

Prof. Rodolfo Bonifacio (Director)
Prof. Fulvio Parmigiani (Supervisor)

Contents

Chapter 1

Introduction

1.1 Overview

In recent years, the advent of ultrashort coherent pulses allowed to investigate solid-state physics in the femtosecond timescale. Nowadays time-resolved spectroscopies are the leading techniques to study different topics such as transient processes in electron gases with reduced dimensionality, photoinduced chemical reaction at surfaces, ultrafast solid-solid phase transitions and strongly correlated systems. At present, shorter excitation pulses, to investigate electronic processes occurring on the attosecond timescale and higher probing photon energies, to study, via femtosecond x-ray diffraction, ultrafast structural dynamics, represent the frontiers of this research field.

In particular, ultrashort pulses have been widely used to extend the photoemission spectroscopy to the non-linear regime. By this technique, it is possible to selectively populate empty states in solids and to study, in the time-domain, the electron relaxation dynamics. An interesting playground to study the electron dynamics at solid surfaces is represented by Image Potential States (IPS). IPS are a transient two-dimensional electron gas interacting with the underlying bulk electrons. For this reason, experiments on IPS constitute a bench mark for current many-body theories concerning the description of a charge at a metal-vacuum interface.

In addition, the excitation of solid systems with ultrashort pulses plays a fundamental role in the study of novel materials. Light pulses can be used to induce electronic and structural phase transitions in molecular crystals or in strongly correlated systems. The investigation of the physical mechanisms, responsible for the solid-solid ultrafast transitions and for the relaxation dynamics that follows, is mandatory to understand the electronic properties of these materials.

The aim of this thesis is to demonstrate the possibility to achieve optical control of electron interactions and phase transitions in specific systems, by selecting the appropriate excitation channels. We have applied this technique to investigate IPS on Ag and the Insulator-Metal phase transition of VO_2.

- The investigation of the IPS on Ag, is performed through two-photon photoemission spectroscopy. We demonstrate that it is possible to populate IPS via different mechanisms, by tuning the photon energy of the excitation light. In addition, the properties of IPS are found to change, due to many-body electron interactions, when a high-density non-equilibrium population is photoinduced in the empty bulk states. This result allows to consider IPS as a probe of the non-equilibrium bulk electronic properties of Ag.
- VO_2 is an interesting metal oxide exhibiting a Insulator-Metal phase transition (IMPT) at T_c=340 K. It has been recently demonstrated that the IMPT in VO_2 can be photoinduced by femtosecond light pulses. We investigate this system by time-resolved reflectivity measurements. Our results clarify the physical mechanism responsible of the photoinduced phase transition and constitute a contribution towards the understanding of the long-discussed electronic properties of VO_2.

1.2 Outline

This work consists of two main sections.

The first section is constituted by Chapters 2, 3, 4. In Chapter 2, the Image Potential

States on Ag are investigated through resonant two-photon photoemission spectroscopy. The results obtained call for a further theoretical investigation of the IPS relaxation mechanisms at the Ag(100) surface.

In the third chapter the photoinduced non-equilibrium electron population in the bulk states is studied via time-resolved multi-photon photoemission spectroscopy. The mechanisms responsible for the energy and momentum conservation during the absorption and photoemission processes are evidenced and discussed. In addition, direct measurement of the relaxation dynamics of the non-equilibrium electrons is performed. The results are in agreement with Fermi-liquid theory and indicate that the photoinduced non-equilibrium population weakly perturbs the Fermi-Dirac electron distribution.

In Chapter 4 the interaction between IPS and the non-equilibrium electron population is probed by means of angle-resolved multi-photon photoemission spectroscopy. Many-body electron interactions are demonstrated, for the first time, to play an important role in the IPS non-equilibrium properties. In this frame, IPS coexisting with the non-equilibrium electron population constitute a powerful model of a two-dimensional electron gas, interacting with a transient three-dimensional electron gas, whose density can be externally controlled.

The second section is developed in Chapter 5. The photoinduced Insulator-Metal phase transition of VO_2 is investigated through time-resolved reflectivity spectroscopy in the near-IR spectral region. We evidence the collapse of the insulating band-gap on the $\sim$100 fs timescale. This result constitutes the first direct evidence that an electronic phase transition coexists with the structural phase transition, induced by laser irradiation. In addition we demonstrate that, by tuning the photon energy, it is possible to decouple two competing excitation channels, represented by the photoinduced hole-doping in the correlated d-band and the impulsive excitation of coherent phonons. In this way we clarify the physical mechanism responsible of the ultra-fast transition.

Chapter 2

Two-Dimensional Electron Gas: Image Potential States on Ag(100)

Image Potential States (IPS) are a particular class of empty surface states originated by electrons trapped at a metal-vacuum interface. They represent an interesting example of a two-dimensional electron gas and the knowledge of the effective masses and lifetimes of the IPS is important to investigate the dynamics of electrons at the surface of metallic systems.

We measure the effective masses of the IPS on Ag(100) by non-linear resonant photoemission spectroscopy. Our data constitute an improvement of the data previously available. In addition the IPS lifetimes are estimated through the line-shape broadening. The measured values open further theoretical investigations concerning the interplay between competing IPS decay mechanisms, in different metallic systems, where the *s*-*d* hybridization and electron correlations effects are present.

2.1 Introduction

Image-potential states (IPS) are an interesting class of surface states on metallic systems, with important implications in advanced surface science, fundamental quantum mechanics and electrodynamics [1, 2, 3]. Electrons populating IPS constitute a transient bidimensional free electron gas localized within a few Angstroms away from the surface. For this reason IPS are a powerful tool to investigate the relaxation dynamics of electrons on metallic surfaces (for a comprehensive review see Ref. [4]), the electron solvation at a metal/polar-adsorbate interface [5] and, more in general, an important model system for many-body theories [6, 4].

Tunable ultra-short laser pulses are generally used to investigate IPS. By exciting the sample with a laser pulse at the appropriate photon energy (pump pulse), it is possible to directly excite electrons from occupied bulk states to unoccupied IPS. By probing the IPS population through a second pulse (pump pulse), the dynamics of electron relaxation is accessible in the time-domain.

An important test for the assumptions used in the theory is the measurement of the image-potential electron effective mass. Previous measurements [7, 8] were based on inverse photoemission technique. In this case insufficient energy resolution prevented the observation of single image potential states and thus accurate effective mass estimates. By means of two-photon photoemission spectroscopy (2PPE) we are able to measure, with great accuracy, the IPS effective masses, along two different directions of the surface Brillouin zone. Our data significantly improve the agreement between the experiments and the predictions from first principle calculations [9].

Besides the accurate measurement of the electron effective masses, information about the relaxation dynamics of electrons populating IPS are important to understand the physics of the IPS. The lifetime of IPS is related to the interaction with the underlying three-dimensional bulk electron system. Due to the little spatial overlap between the IPS wavefunctions (localized outside the surface) and the bulk electron wavefunctions, the typical lifetime is of the order of 50-100 fs. For this reason it is possible to investigate the IPS dynamics both through line-shape broadening and, in the time-domain, through pump-probe techniques. Lifetime measurements on Cu(100), performed with time-resolved photoemission, have been recently demonstrated that the dependance of the IPS lifetime on the momentum parallel to the surface is a fingerprint of the physical mechanism responsible of the decay [6]. At this light our results on the intrinsic linewidth broadening as a function of the momentum parallel to the surface, give interesting information about the relaxation dynamics at the Ag(100) surface.

2.2 A particular class of surface states: Image Potential States

Image Potential States are originated by electrons trapped in front of a metal surface when a gap of the projected bulk states occurs at energies below the vacuum level. In this case the little spatial overlap between the IPS wavefunctions (localized outside the surface) and the bulk electron wavefunctions, prevents electrons from decaying into the bulk and a long range binding potential is formed by the Couloumbic attraction between electrons in the vacuum and their image charge in the solid. Along the z direction, perpendicular to the surface, the binding hydrogenlike potential is given by:

$$V(z) = E_{vac} - \frac{e^2}{4\pi\epsilon_0}\frac{1}{(4z)} \tag{2.1}$$

whereas the electron is unbound in the x-y plane parallel to the surface. The eigenvalue problem factorizes in a 2-dimensional free-electron like wavefunction parallel to the surface plane and a bound hydrogen-like wavefunction along the z direction perpendicular to the surface. The wavefunctions for the perpendicular direction are obtained from the radial part of the wavefunctions for the hydrogen atom multiplied by z (due to the reduced dimensionality) and expanded by a factor 4 (due to the weaker potential) [10] (see Fig. 2.1). An attempt to explain IPS based on a simple analytical model [11] predicts a universal Rydberg-like binding energy $E(n) = -Ry/16n^2 = -0.85(eV) \cdot n^{-2}$ and a lifetime τ_n that scales as τ_n=n^3, where $n = 0, 1, 2, \ldots$. The Rydberg-like states are called Image Potential States and, for a fixed value n, constitute a two-dimensional free electron gas, with a maximum of the probability density typically of several Angstroms away from the metal surface and increasing quadratically with the quantum number n.

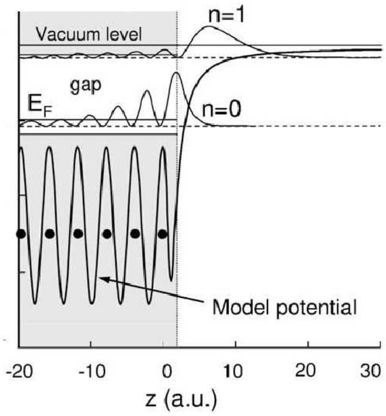

FIGURE 2.1: A schematic picture of the projected bulk states and the surface-states wavefunctions along the z direction is shown for a system characterized by an occupied intrinsic surface state (n=0) and an unoccupied IPS (n=1). The n=0 and n=1 eigenvalues are represented by the dotted line and fall in the energy gap. The maximum of the probability density of the wavefunction of the n=1 IPS is a few Angstroms away from the surface, whereas the maximum relative to the n=0 state is situated on the z=0 plane. The shaded areas indicate the projected bulk bands along a particular direction of the Brillouin zone. The black line, oscillating in the bulk and hydrogen-like in the vacuum, is a model of the potential experienced by electrons, whereas the dots give the positions of the atomic planes. The figure has been taken from [11].

However, significant disagreements are found when the predictions of this model are compared to experiments [12]. To resolve this discrepancy, corrections to the Rydberg-like formula have been devised [13] and first principles calculations, with accurate estimates of the potentials in the bulk and at the metal surface, have been developed [9].

IPS have been studied in the last years both from a theoretical and from an experimental point of view on different metallic surfaces, such as C(0001), Ni(111), Cu(100) and Cu(111), Ag(100) and Ag(111), Pd(111), Pt(111), Ru(0001) and Li(110) [4]. The recent growing interest in this class of surface states is due to the fact that they constitute a unique tool to investigate electron dynamics at surfaces and to test the current many-body theories, describing the dynamics of electrons on IPS by self-energy calculations.

2.3 Angle-resolved non-linear resonant photoemission from Image Potential States

2.3.1 *Non-linear photoemission spectroscopy*

In the last years an intense effort has been dedicated to investigate the quantum mechanical and symmetry properties of image-potential states using a variety of experimental techniques, such as low-energy-electron diffraction [14], inverse photoemission [15], scanning-tunneling microscopy [16] and, more recently, two-photon photoemission spectroscopy [17].

Standard photoemission constitutes a technique widely used to map the occupied electronic bulk states. In fact if a sample is irradiated with electromagnetic radiation with a photon energy $h\nu$ greater than the work function Φ of the material, electrons will be photoemitted at a kinetic energy E_{kin}, given by:

$$E_{kin} = h\nu - \Phi \tag{2.2}$$

As a consequence, the photoemission spectrum is a picture of the occupied bulk states, under the assumption that final states form a smooth continuum and the transition probability is homogeneous. The energy range that can be investigated with this technique is limited to occupied initial states, i.e. states with an energy smaller than the Fermi energy E_F, and empty final states at energy above the vacuum level $E_{vac} = E_F + \Phi$. As a consequence unoccupied states, such as surface or image potential states, can not be studied by means of linear photoemission.

With the advent of high-intensity ultrashort laser pulses, it is now possible to investigate photoemission processes in the non-linear regime, when $h\nu < \Phi$. By tuning the photon energy of incident light, normally empty IPS states below the vacuum level can be populated via 1-photon absorption, and, upon the absorption of a second photon, electrons can be photoemitted from IPS. The image potential states constitute a strong resonance with respect to non-linear processes, resulting in a well defined spectral feature in the non-linear photoemission spectrum.

In Fig. 2.2 the 2-photon photoemission process on Ag(100) is schematically shown. The binding energy of the n=1 and n=2 IPS on Ag(100) is E_1=0.53 eV and E_2=0.15

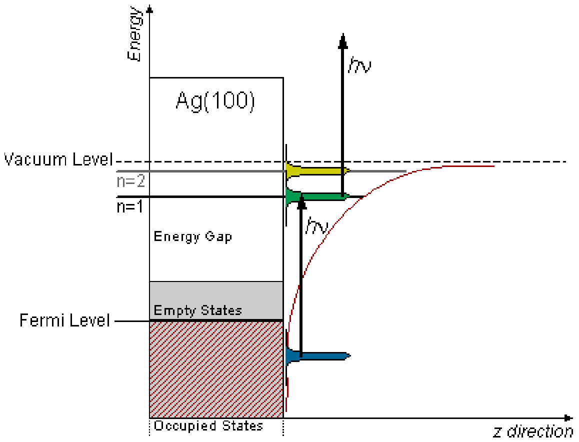

FIGURE 2.2: A schematic picture of the energy levels at the Ag(100) surface is shown. The work function $\Phi = E_{vac} - E_F$ is about 4.3 eV and the binding energies of the n=1 and n=2 IPS are E_1=0.53 eV and E_2=0.15 eV, respectively [18, 19]. When the photon energy is about 4 eV, it is possible to perform resonant 2PPE spectroscopy on IPS. The energy scale has been deformed for graphical reasons.

eV, respectively [18, 19]. It is thus possible to perform 2PPE on these states by tuning the photon energy at a value of about 4 eV, smaller than the work function Φ=4.3 eV, but sufficient to directly populate IPS from occupied bulk states (the energy difference between the Fermi level and the n=1 IPS is about 3.8 eV).

2.3.2 *Angle-resolved photoemission spectroscopy*

Angle-resolved photoemission spectroscopy (ARPES) is, in general, a photoemission technique which allows to investigate the dispersion of the electronic energy bands $E_n(k_{\parallel}^{int})$ as a function of the momentum parallel ($k_{\parallel}^{int}$) to the sample surface of the electrons inside the bulk. In fact, as a consequence of two-dimensional translational symmetry, the wave-vector component parallel to the surface is conserved in the transition from the occupied states to the vacuum: $k_{\parallel}^{int}$=$k_{\parallel}^{ext}$ where $k_{\parallel}^{ext}$ is the momentum component parallel to the surface of photoemitted electrons. The $k_{\parallel}$ momentum can thus be calculated by the expression:

$$k_{\parallel} = \frac{\sqrt{2mE_{kin}}}{\hbar} \sin\theta \tag{2.3}$$

where E_{kin} is the photoelectron kinetic energy and m is the electron rest mass.

This technique can be successfully applied in the case of image potential states. In fact, due to the reduced dimensionality of the IPS free electron gas, it is possible to reconstruct the dependance of the IPS binding energy as a function of $k_{\parallel}$. In the case of parabolic-like dispersion, it is also possible to estimate the value of the electron effective mass m^*, by fitting the measured dispersion with a quadratic function of $k_{\parallel}$:

$$E_n(k_{\parallel}) = \frac{\hbar^2 k_{\parallel}^2}{2m^*} \tag{2.4}$$

where m^* is a fitting parameter.

2.4 Experimental set-up

In this section a description of the experimental set-up developed for angle-resolved non-linear photoemission experiments is reported. As evident by the schematic drawing of Fig. 2.3, the experimental arrangement consists of three main stages: the laser source, the ultra-high vacuum chamber, fully equipped for sample preparation and analysis, and the electron detector.

The light source is constituted by a travelling-wave optical parametric generator (TOPG) pumped by an amplified Ti:Sapphire laser system, in order to obtain a broad tunability of the photon energy. In the TOPG, a pump beam (λ_{pump}=790 nm) is converted on a BBO crystal into a *signal* and an *idler* beam, through a non-linear interaction. Due to the energy conservation, the relationship between the pump, *signal* and *idler* wavelengths (respectively λ_{pump}, λ_{signal} and λ_{idler}) is given by:

$$\frac{1}{\lambda_{pump}} = \frac{1}{\lambda_{signal}} + \frac{1}{\lambda_{idler}} \tag{2.5}$$

The output of the TOPG is a train of 150 fs-pulses at 1 kHz repetition rate and with an average power of about 50 mW. The *signal* of the TOPG is constituted by radiation with

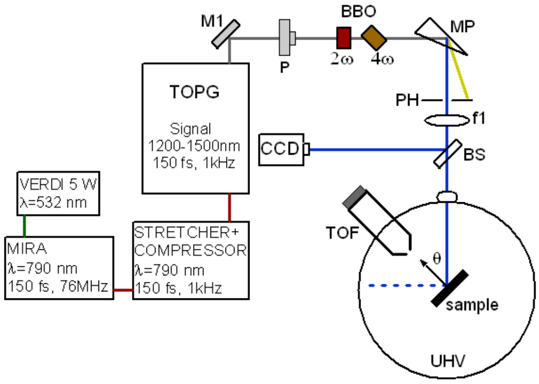

FIGURE 2.3: A schematic drawing of the experimental set-up, constituted by three main stages: the laser source (TOPG), the ultra-high vacuum chamber (UHV) and the time of flight spectrometer (TOF). For a detailed explanation refer to section 2.4.

tunable wavelenght in the range of 1600-1200 nm (0.78-1 eV), whereas the wavelength of the *idler* (the radiation associated to the parametric down-conversion in the TOPG) spans the range 2400-1600 nm (0.51-0.78 eV). The output of the TOPG is directed to the experimental chamber through an optical path, optimized for the quadruplication of the *signal*: the *idler*, reflected by the mirror **M1** together with *signal*, is stopped through a polarizer **P**; the *signal* is then quadrupled by means of two **BBO** crystals and is focalized on the sample inside the chamber through a lens of focal length **f1**. Before entering the vacuum chamber, the light is dispersed by a prism with a Al-coated side (**MP**) and filtered by a pin-hole **PH**, in order to separate the fourth harmonic from the *signal* and its second harmonic. A beam splitter (**BS**) is also used to monitor the beam profile through a 14-bit **CCD** camera.

The experiments are carried out in a μ-metal ultrahigh vacuum (**UHV**) chamber system with a base pressure of 5×10^{-10} mbar at room temperature. The sample is a Ag single-crystal oriented along the (100) surface with an error of $\pm 2^\circ$ and its surface is cleaned by cycles of Ar^+ sputtering and subsequent annealing at 400 K. The surface quality is tested with low-energy electron diffraction (LEED) analysis. However, a bright and sharp LEED does not guarantee the needed surface standard to perform the experiment. The cleaning procedure should be carried on till the proper work function for Ag(100) is obtained. The value of the work function is usually measured via direct photoemission, using the forth harmonic of the Ti:Sapphire fundamental radiation (λ=200 nm, $h\nu = 6.28\ eV$) and results to be $\Phi = 4.3 \pm 0.1$ eV. The sample is hold by a 5-degrees of freedom manipulator, which can be cooled down at about 100 K.

The kinetic energy of the photoemitted electrons is measured by a time of flight (**TOF**) spectrometer [20] mounted in the μ-metal UHV chamber. The residual magnetic field inside the chamber is smaller that 10 mG and the TOF length is about 440 mm. The photoelectrons are detected by a pair of multi-channel plates mounted in chevron configuration and the arrival time is recorded by a multi-hit time-to-amplitude converter with 0.5 ns resolution. The overall temporal resolution of the detection chain is 1 ns. The diameter of the multi-channel plate is 40 mm, resulting in a geometrical acceptance angle of ± 2.6 °. The energy resolution is expected to be about 30 meV at a kinetic energy of 2 eV. The UHV chamber is also equipped with another TOF spectrometer, characterized by higher resolution with respect to the detector used for the measurements reported in this chapter. In particular, the high-resolution TOF has an angular acceptance of ± 0.83 ° and is equipped with a 0.25 ns-resolution time-to-amplitude converter. This TOF has been used to investigate the influence of the angular resolution on the linewidth measurements, as discussed in detail in Appendix A.

2.5 Results and Discussion

2.5.1 Effective mass of electrons on IPS of Ag(100)

The values of the image-potential effective masses are directly related to the potential experienced by electrons in the metal-vacuum interface: any variation from unity is the fingerprint of an influence on the electronic properties of the potential parallel to the surface. For this reason the IPS effective masses constitute a crucial parameter for the theoretical models investigating this problem.

Table 2.1 reports the data of the $n = 1$ image state effective mass on Ag(100), available

Table 2.1: Measured and calculated electron effective mass (in free electron mass units m*/m) for the n=1 and n=2 image potential states on Ag(100).

Measured values		Calculated values	
$n = 1$	$n = 2$	$n = 1$	$n = 2$
1.6 ± 0.3[1]	1.06 ± 0.09[2]	0.95[3]	1.03[4]
1.2 ± 0.2[5]	1.03 ± 0.06[6]	1.03[4]	
1.15 ± 0.1[3]		1.0[7]	
0.99 ± 0.02[2]			
0.97 ± 0.02[6]			

1)Reference [8]
2)This work, measured along $\bar{\Gamma}\bar{M}$.
3)Reference [13]
4)Reference [9]
5)Reference [7]
6)This work, measured along $\bar{\Gamma}\bar{X}$.
7)Reference [12]

in literature. At the best of our knowledge no data are available for the state $n = 2$. The measurements reported in Ref. [7, 8], were based on inverse photoemission spectroscopy. The insufficient energy resolution of this technique prevented the observation of single image potential states and thus accurate effective mass estimates. More recently 2PPE spectroscopy has been used to investigate IPS properties, improving the accuracy of the IPS effective mass measurements [13].

A high resolution 2PPE spectrum with the $n = 1$ and $n = 2$ image states is reported in Fig. 2.4. The spectrum is obtained using 150 fs laser pulses at a photon energy of 4.32 eV. The incident radiation is p-polarized (electric field parallel to the plane of incidence) and the incidence angle is 30 °. The electrons are detected along the normal to the sample surface ($k_{\parallel}$=0). In accordance to the selection rules [21], the image potential features are not observable with s-polarized light (electric field normal to the plane of incidence). The

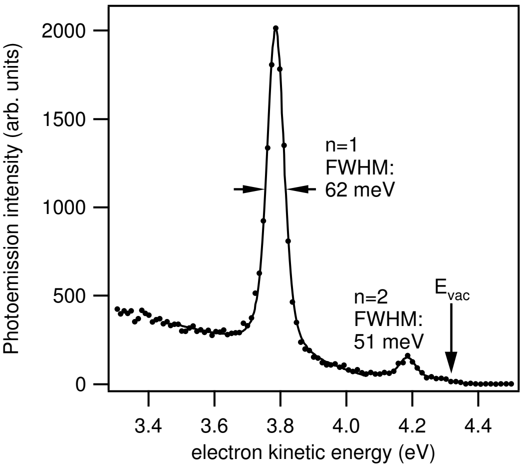

FIGURE 2.4: A high resolution 2PPE spectrum with the $n = 1$ and $n = 2$ image states is reported. The line is the fit of IPS with a Lorentzian profile convoluted with a Gaussian representing the energy resolution. The Full-Width-Half-Maximum (FWHM) of the Gaussian is about 45 meV (for a detailed discussion, see Appendix A). The deconvoluted intrinsic linewidth of the Lorentzian is 14 ± 2 meV for $n = 1$ and 6 ± 6 meV for $n = 2$. The spectrum is taken at normal emission ($k_{\|}$=0) on a Ag(100) single crystal, irradiated by 150 fs-laser pulses, with a photon energy $h\nu = 4.32$ eV. The angle of incidence is 30 ° with a p-polarized incident light.

spectral amplitude of the $n = 1$ image state associated with IS1 has a peak to background contrast ratio of about 8:1. This is much higher than the 2:1 contrast obtained with 10 ns pulses, indicating an efficient photoemission mechanism from the image state, even if a surface state to be used as a resonant enhancement is not present in the (100) direction of silver (see discussion in Ref. [19]). Since the lifetime of the $n = 1$ image potential state on silver is less than 100 fs, the use of pulses in the 100 fs range provides a decisive advantage with respect to signal level in two-photon photoemission. On the other hand, the use of short pulses limits the attainable spectral resolution due to finite pulse spectral width (laser pulse spectral width is 12 meV in our case).

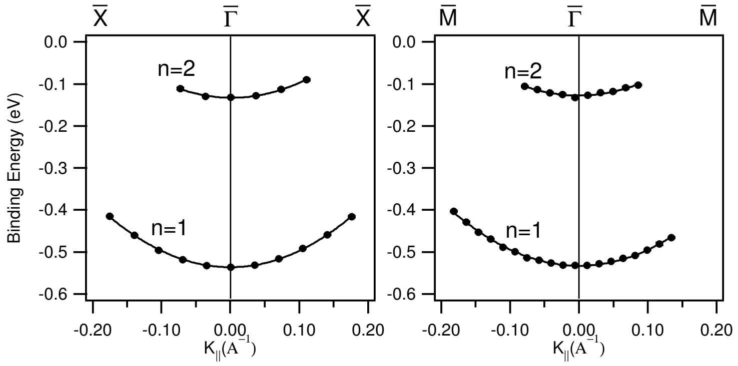

FIGURE 2.5: Binding energy versus $k_\parallel$ dispersion for the $n = 1$ and $n = 2$ image potential states measured with two-photon photoemission on Ag(100). The data points are fitted by parabolas (lines). The binding energies at $\bar{\Gamma}$ are 530 ± 50 meV for $n = 1$ and 130 ± 50 meV for $n = 2$ [19].

The photoemission measurements are carried out along the two symmetry directions of the Ag(100) SBZ. One is for light incident in the bulk ΓLUX mirror plane, i.e. along the $\bar{\Gamma}\bar{X}$ direction, the other for light incident in the bulk ΓXWK mirror plane, i.e. along the $\bar{\Gamma}\bar{M}$ direction. The work function (Φ) is estimated using the low-energy electron cutoff of the spectrum (E_{kin}^{low}). In this case Φ is connected to the spectral parameters by the relation $\Phi = h\nu - E_{kin}^{max} + E_{kin}^{low}$, where E_{kin}^{max} is the high-energy cutoff of the spectrum. A work function of $\Phi = 4.3 \pm 0.1$ eV is obtained from these measurements, in agreement with the value obtained through direct photoemission (see section 2.4).

The peak position and intrinsic linewidth of the IS1 and IS2 distribution curves are calculated with a fit of a convolution of a lorentzian with a gaussian (see Fig. 2.4). The gaussian represents an approximation to the apparatus resolution (spectrometer resolution + laser linewidth + geometrical aberration due to finite laser spot area), and it is set to 45 meV FWHM. Convergence of the fit is obtained by a χ^2 minimization.

The effective mass $m^* = \hbar^2/(d^2E/dk_\parallel^2)$ associated with the electrons in the first two image potential states at $\bar{\Gamma} = 0$ is measured by a parabolic fitting of the energy versus wave-vector position of the peaks of the $n = 1$ and $n = 2$ image states features (see

Fig. 2.5). The momentum parallel to the surface is given by $k_{\parallel} = \sqrt{2mE_{kin}} sin(\theta)/\hbar$, with θ measured from the sample normal. The geometrical acceptance angle of the ToF implies a spread in $k_{\parallel}$ given by $\Delta k_{\parallel} = \pm 0.05 \mathring{A}^{-1}$. At a specified angle, electrons with different parallel k-vectors are collected simultaneously and each spectrum represents a weighted average of such a distribution. To evaluate the influence of the k-vectors spread on the curvature of the quasi-free electron parabola, a simple boxcar averaging with $\Delta k_{\parallel}$ spread on a free electron parabola has been performed. The effective mass m^*/m variation is less than 0.002. In the errors reported for the effective mass this effect has been taken into account. Along the $\bar{\Gamma}\bar{M}$ direction we measured $m^*/m = 0.99 \pm 0.02$ for the $n = 1$ state and $m^*/m = 1.06 \pm 0.09$ for $n = 2$. Along the $\bar{\Gamma}\bar{X}$ direction the result is $m^*/m = 0.97 \pm 0.02$ for the $n = 1$ state and $m^*/m = 1.03 \pm 0.06$ for $n = 2$. Even if theoretical predictions do not specify a dependence on the SBZ direction of the effective mass, these values are in agreement, within the experimental errors, with first principle calculations [9] and with the phase-shift analysis [13]. This result demonstrates that the image states in Ag can be regarded as nearly free electron states and that corrugation or irregularity of the potential parallel to the surface do not play a significant role. For a comparison of the measured and calculated effective masses for Ag(100), see Table 4.1.

2.5.2 Intrinsic linewidth and lifetime at $k_{\parallel}$=0

Besides the accurate measure of the electron effective masses, information about the dynamics of image-states obtained from intrinsic linewidth analysis are important to understand the physics of the IPS. In fact, in recent years, current many-body theories have been applied to the calculation of the relaxation lifetime of IPS, thereby constituting an important tool for the interpretation of the experimental results. A particular theoretical investigation was dedicated to the problem of the relaxation dynamics of IPS on Ag(100). In fact for Ag(100) a very fast decay time was expected, as compared to the case of Cu(100), due to the presence of a surface plasmon decay channel. On the contrary, the first direct measurements of the lifetimes of IPS on Ag(100) [22] gave results very similar to the case of IPS on Cu(100). This discrepancy between theory and results led to a further theoretical investigation of IPS dynamics on Ag(100).

TABLE 2.2: Measured and calculated lifetimes of the $n = 1$ and $n = 2$ image potential states on Ag(100).

Measured values (fs)		Calculated values (fs)	
$n = 1$	$n = 2$	$n = 1$	$n = 2$
55 ± 5^1	160 ± 10^1	26.5^2	132^2
25 ± 10^3	180 ± 20^3	55^4	
31 ± 6^5	$\geq 66^5$		
47 ± 7^6	$\geq 55^6$		

1)Reference [22]
2)Reference [25]
3)Reference [21]
4)Reference [24]
5)Reference [26]
6)This work (lifetimes deduced from measured intrinsic linewidths $\tau = \hbar/\gamma$)

To rationalize this behavior, we follow the models reported in Refs. [23, 24]. The significant result given in Ref. [23] regards the effect of spatially varying *s*-*d* screening on the quasi-particle dynamics at Ag surfaces. The main excitation mechanisms included are the creation of electron-hole pairs and collective modes induced by gradients of the time-varying fields at the surface region. The interplay between *s*- and *d*- electron densities in the *s*-electron spill out region leads to a weaker *s*-*d* screening and consequently to a larger imaginary self-energy, i.e. a quasi-particle damping significantly larger than in the bulk. A subsequent elaboration of the same model focused on Ag(100) surface [24], explains the discrepancy between measured relaxation of the $n = 1$ image state at $k_{\parallel} = 0$ and the calculated values. The conclusion states that, although the imaginary part of the self-energy is enhanced because of the presence of the surface plasmon decay channels, the interference resulting from the non-locality of the self-energy leads to a longer overall image-state lifetime.

In the following discussion a connection to the lifetimes (τ) of the IPS is made through

$\tau = \hbar/\gamma$ ($\hbar = 658$ meV fs) in order to compare our results with experiments measuring lifetimes using pump and probe techniques [21, 12, 22, 6].

The lineshape analysis of the $n = 1$ and $n = 2$ at $\bar{\Gamma}$ gives intrinsic linewidths (and the associated lifetime) that compare well with those reported in the literature (see Table 2.2). The measured values are $\gamma_1 = 14 \pm 2$ meV for the $n = 1$ state (see Fig. 2.4) and $\gamma_2 = 6 \pm 6$ meV for the $n = 2$ state. To estimate the lifetime of the $n = 1$ image state, the linewidth analysis has an accuracy comparable to that obtained by time resolved two photon photoemission (TR2PPE). The real advantage of TR2PPE is seen in measuring the lifetime of the longer lived (n greater than 2) image states (see Table 2.2). These states have intrinsic linewidths of few meV that cannot be reliably measured due to limited energy resolution of electron spectrometers. It is important to underline that, in general, time-resolved lifetime measurements are sensible only to the electron population density of a state. No information about processes, such as elastic scattering, which do not change the number of electrons on a particular energy level is attainable with this technique. On the contrary, intrinsic-linewidth measurements give information about all the decaying channels. For this reason the similarity between our results and the results obtained via time-resolved photoemission, indicates that, at $k_{\|}$=0, elastic scattering mechanisms do not play an important role.

2.5.3 Intrinsic linewidth and lifetime at $\mathbf{k}_{\|} \neq 0$

Recently it has been demonstrated that the study of the dependance of the IPS lifetime on the momentum parallel to the surface gives information about the scattering mechanisms involved in the decay process [6]. In particular the relaxation processes, due to the overlapping between the image state wave function and bulk states [27], can be classified in *interband* and *intraband* processes. The final state of the *intraband* process is an IPS state whereas the final state of the *interband* decay channel is a bulk state (see Fig. 2.6). As a general rule, a broadening of the intrinsic linewidth with respect to normal emission ($k_{\|}$=0) is observed when a IPS is measured at a parallel momentum different from zero. From a theoretical point of view, the lifetime τ is found to depend on $k_{\|}$ in a different way for *interband* and *intraband* processes. In this frame knowledge of the intrinsic linewidth

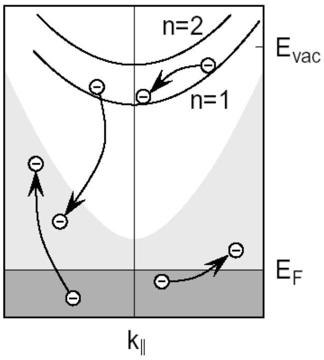

FIGURE 2.6: A schematic picture of the scattering processes responsible of the decay of electrons on IPS is shown. On the right: *intraband* mechanism when the electron final state is an IPS state. On the left: *interband* mechanism when the electron final state is a bulk state. The picture has been taken from [4].

as a function of parallel momentum helps in discriminating which mechanism contribute to the IPS decay.

A plot of the measured intrinsic linewidths and associated lifetimes of the $n = 1$ image state as a function of the kinetic energy of parallel motion $E_{\|} = \hbar^2 k_{\|}^2/2m$ is shown in Fig. 2.7. In the graph the error bars refers to the uncertainty arising in the determination of the lifetime from the fitting procedure to the single linewidth. To give an estimate of the influence of sample preparation and the overall repeatability of the experiment, separate sets of measurements are shown in Fig. 2.7. The influence of $\Delta k_{\|}$ resolution on the inverse linewidth measurements is discussed in detail in Appendix 1, where a new fitting procedure is proposed and compared with results obtained with the high resolution TOF (see section 2.4).

The intrinsic linewidth γ_1 =14 meV (corresponding to a lifetime of $\approx$ 50 fs) at $k_{\|} = 0$ rapidly increases to more than 50 meV (lifetimes of the order of 10-15 fs) for values of $E_{\|} \geq 0.13$ eV, corresponding to $k_{\|} \geq 0.18\mathring{A}^{-1}$.

The solid line in Fig. 2.7 is a linear estimate of the $n = 1$ state intrinsic linewidth versus $E_{\|}$ using a slope $S = 300$ meV/eV and $\gamma(k_{\|} = 0) = 14$ meV. By taking into account the

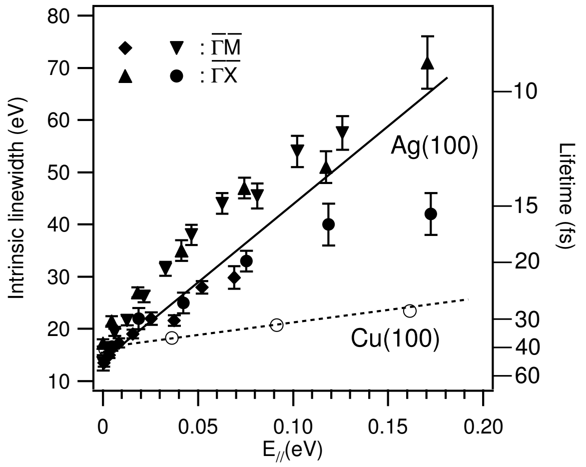

FIGURE 2.7: Experimental intrinsic linewidths (left axis) and associated lifetimes (right axis) of the first image state in Ag(100) as a function of the excitation energy $E_{\parallel} = \hbar^2 k_{\parallel}^2/2m$ (filled dots). Solid line: intrinsic linewidth linear estimate of data with a slope $S = 300$ meV/eV and $\gamma(k_{\parallel} = 0) = 14$ meV. Empty circles: lifetimes measured on Cu(100), from Ref. [6]. Dashed line: linear estimate of Cu(100) data using the values $S = 47$ meV/eV and $\gamma(k_{\parallel} = 0) = 16.5$ meV.

influence of the geometrical angular acceptance of the detector, as described in Appendix 1, the value of the slope of line fitting the data in Fig. 2.7 is reduced to $S = 115 \pm 30$ meV/eV.

The intrinsic linewidth broadening of the Ag(100) image-potential state, as $E_{\parallel}$ increases, is significantly larger when compared to the inverse lifetime ($\hbar/\tau$) broadening measured on Cu(100). The dotted line in Fig. 2.7 is obtained from a linear fit of intrinsic linewidths measured in Cu(100) using the values [6]: $S = 47$ meV/eV and $\gamma(k_{\parallel} = 0) =$ 16.5 meV.

In this framework, our results indicate that the mechanism leading to interference effects, related to the non-locality of the self-energy and resulting in a long image-state lifetime ($\tau \simeq 50$ fs) is less effective at $k_{\parallel} \neq 0$. This could explain the much more rapid decay of the lifetime in Ag with respect to Cu assuming that the intrinsic linewidth is governed only by energy relaxation processes. Another possible contribution to the observed linewidth broadening with parallel momentum increase is quasi-elastic intra-band electron scattering. However, to determine the role of such phase-destroying scattering mechanisms on the present measurements, further experimental and theoretical investigations are necessary.

2.6 Summary

The effective electron masses for the n=1 and n=2 image-potential states on Ag(100), are measured along the $\bar{\Gamma}\bar{M}$ and $\bar{\Gamma}\bar{X}$ directions of the surface Brillouin zone, through resonant two-photon photoemission spectroscopy. The measured values constitute an improvement of the agreement between the experiments and the theoretical predictions. In addition, the intrinsic linewidth of IPS, as a function the momentum parallel to the surface, has been obtained from line-shape analysis of angle-resolved two-photon photoemission spectra. For the $n = 1$ state the measured intrinsic linewidths have been observed to increase from 14 meV at normal emission ($k_{\|} = 0$) to 70 meV at $k_{\|} = 0.18\AA^{-1}$. This findings, when compared to the significantly lower inverse lifetime broadening measured on Cu(100), open the question of the interplay between collective particle effects and non-local mechanisms associated to the image-potential electrons decay dynamics.

Chapter 3

Photoinduced Non-Equilibrium Electron Dynamics in Metals

When a metal is irradiated by ultrashort coherent pulses, with a photon energy smaller than the work function, a non-equilibrium electron population is created in the conduction band. The study of the dynamics of electrons photoexcited in the bulk empty states is mandatory to understand in depth the physics of electronic systems in the highly non-equilibrium regime.

We perform non-linear photoemission spectroscopy on Ag(100). We report on the experimental evidence that a scattering mechanism is responsible of the momentum conservation during the absorption and photoemission processes. Time-resolved measurements show that, at low laser intensities, the relaxation dynamics of the non-equilibrium electrons is in agreement with Fermi-liquid theory, and weakly perturbs the Fermi-Dirac bulk electron distribution.

3.1 Introduction

Non-linear photoemission processes, can be investigated by exciting a metal with ultrashort laser pulses. When the photon energy ($h\nu$) is smaller than the work function (Φ) of the sample, the maximum kinetic energy of photoemitted electrons is expected to be:

$$E_{kin} = nh\nu - \Phi \tag{3.1}$$

where n is an the minimum number of photons necessary to overcome the work-function energy barrier. On the contrary non-linear photoemission spectra are generally characterized by a high energy electron tail [28, 29, 30, 31, 32], i.e. by electrons with a kinetic energy $E_{kin} > nh\nu - \Phi$. The physical mechanisms producing this peculiar feature are not well understood, but there are evidences that an important role is played by the non-equilibrium electron population created in the conduction band by the absorption of the ultrashort laser pulses [32, 33]. For this reason the investigation of the dynamics of the non-equilibrium electron population in metals is mandatory to understand the influence of the photoexcited free-electron gas on the non-linear photoemission processes.

In this chapter we analyze the non-linear photoemission spectra obtained by irradiating an Ag(100) single crystal with 3.14 eV femtosecond laser pulses. The high energy electron tail detected at low laser intensities (I$\simeq$0.1 GW/cm^2), is attributed to a non-thermalized free-electron gas in the metal conduction band. The analysis of the band structure of Ag(100) suggests that the momentum conservation during the absorption and photoemission processes is assured by a scattering mechanism, changing the component of the electron momentum parallel to the surface (k$_{\|}$). At the light of recent theoretical models, the absorption mechanism can be attributed to photon absorption during electron collisions with phonons [34] or to an inverse bremsstrahlung process [35]. In this frame the collected photoemission spectrum is the fingerprint of the non-equilibrium electron distribution in the empty *s-p* bands at k$_{\|}$ different from zero.

To study in the time-domain the relaxation dynamics of the non-equilibrium electron population, we perform pump-probe measurements, which indicate a mean relaxation time faster than 150 fs, for electrons with energy between 0.3 and 2.3 eV relative to the Fermi level. This value is consistent with the lifetime of excited electrons predicted by Fermi-liquid theory [36]. In addition, during the relaxation process, we do not observe a significant increase of the Fermi temperature of the equilibrium electron distribution, in agreement with predictions of the two-temperature model [37, 38]. These results indicate that, at very low laser intensities, we are able to create and detect a non-equilibrium electron population which perturbs in a negligible way the equilibrium electron distribution.

3.2 Time-resolved photoemission spectroscopy on metals

Standard photoemission can be used to map the equilibrium electron distribution in metals. In Fig. 3.1 the linear photoemission process is shown (left): if the photon energy $h\nu$ of the electromagnetic radiation is greater than the work function Φ (Φ=Vacuum Level-Fermi Level) of the material, the photoemission spectrum is a picture of the occupied bulk states. This statement is valid under the assumption that final states form a smooth continuum and the transition probability is homogeneous.

On the other hand if the metal is irradiated with a photon energy $h\nu_1$ smaller than the work function (pump pulse), linear photoemission is suppressed and the electro-magnetic field energy is absorbed by electrons, resulting in the creation of a non-equilibrium population in the conduction band (Fig. 3.1, on the right). If the sample is excited at a time-delay τ by another laser pulse (probe pulse) with a photon energy $h\nu_2$ ($h\nu_2 + h\nu_1 > \Phi$), it is possible to probe the non-equilibrium electron distribution. By changing the delay τ between the pump and probe pulses it is possible to follow in the time domain the relaxation dynamics of excited electrons (this technique is referred to as time-resolved photoemission).

The first direct measurement of the thermalization of the non-equilibrium electron population has been performed through 2PPE on a polycristalline metal film irradiated by femtosecond laser pulses, with an incident fluence larger than 1 GW/cm^2 [39, 40]. Evidence of the heating of the Fermi edge, due to the energy exchange between the high density non-equilibrium population and the Fermi-Dirac bulk distribution, is reported. The measured thermalization time of the free-electron gas resulted as long as 1 ps. On this timescale the role of energy transfer between the non-equilibrium population and the lattice can not be neglected. These results opened the question of the physical mechanism

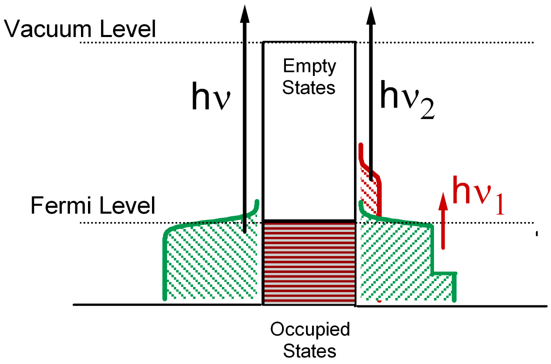

FIGURE 3.1: A schematic drawing of the linear (on the left) and non-linear (on the right) photoemission processes on a metal is shown. Left: when the photon energy $h\nu$ is greater than the work function, the photoemission spectrum is a picture of the equilibrium electron distribution. Right: when the photon energy $h\nu_1$ is smaller than the work function, it is possible to study the dynamics of non-equilibrium electron distribution.

---

responsible of the photo-induced population of the metal conduction band. In fact a direct dipole transition between two levels in the same branch of the *s*-*p* conduction band is forbidden by momentum and energy conservation laws. As a consequence, a deeper theoretical investigation of the energy absorption process and of the influence of the non-equilibrium electron distribution on relaxation dynamics, was carried out in the following years [41, 34, 35].

In this context we have performed time-resolved photoemission spectroscopy on a Ag(100) single-crystal, in order to investigate the photoemission process along a particular direction of the Brillouin zone. In this way we are able to reconstruct the momentum of the electrons parallel to the sample surface and to clarify the mechanism involved in the non-linear photoemission process. A very low laser intensity (I$\simeq$0.1 GW/cm^2) of the pump beam is used in the experiment. As a consequence the measured heating of the Fermi-edge can be neglected.

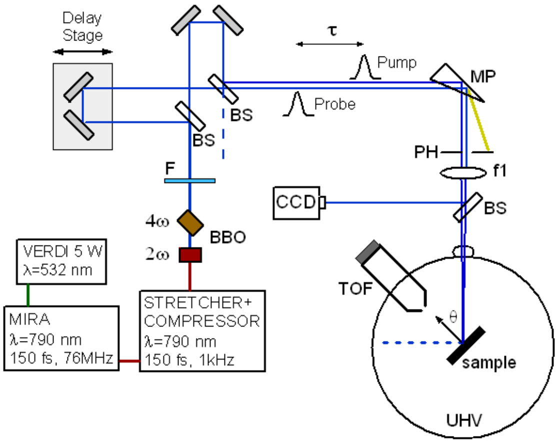

FIGURE 3.2: A schematic drawing of the experimental set-up for time-resolved photoemission. The second harmonic of an amplified Ti:Sapphire laser system is used to excite the sample. A Delay Stage is used to introduce a delay time τ between the *Pump* and *Probe* pulses. The electron detector is a Time of Flight spectrometer (TOF) inside a μ-metal ultra-high vacuum (UHV) chamber. For a detailed explanation refer to the section 3.3.

3.3 Experimental set-up

The experimental set-up for time-resolved non-linear photoemission (see Fig. 3.2) is similar to the one reported in Chapter 1. The light source is an amplified Ti:Sapphire laser system emitting 800nm-150fs pulses at 1 kHz repetition rate. The pump-probe experiment is performed with a photon energy hν=3.14 eV, obtained by duplicating the fundamental radiation with a **BBO** crystal. The fourth harmonic of the fundamental (hν=6.28 eV) is used for direct photoemission measurements, in order to estimate the work function Φ of the Ag(100) sample. A filter **F** is used to eliminate the 790-nm component. The next stage is a Mach-Zehnder interferometer: the laser is divided into two beams through a beam splitter (**BS**); a delay time τ is introduced between the *pump* and *probe* pulses through a Delay Stage, constituted by a linear translator with a minimum step of 40 nm

(0.13 fs); the two pulses are recombined on a beam splitter (**BS**). The two pulses are successively dispersed on a prism with a Al-coated side (**MP**), in order to separate the different wavelenghts and filtered by a pin-hole (**PH**). Finally the *pump* and *probe* pulses are focalized on the same point of the sample inside the UHV chamber. A **CCD** camera is used to monitor the beam-profiles of the two pulses. The size of the spot, about 300x300 μm^2, is chosen in order to have a high count rate minimizing space-charge effects in the photoemission spectra.

The Ag single-crystal, oriented along the (100) surface, is kept in a μ-metal ultra-high vacuum chamber with a base pressure of 2x10^{-10} mbar at room temperature. The sample surface is cleaned and monitored with the procedures described in Section 2.4 of Chapter 2. The measured work function is 4.3±0.1 eV.

The kinetic energy of the photoemitted electrons is measured by the high resolution time of flight (TOF) spectrometer (see Appendix A), characterized by an acceptance angle of ±0.83°. The total energy resolution of the experimental set-up (laser linewidth plus detector resolution) is 35 meV at a kinetic energy of 2 eV.

3.4 Results and Discussion

3.4.1 Non-linear photoemission spectrum: high-energy electron tail

In this section we discuss in detail the non-linear photoemission spectrum obtained on Ag(100), with 3.14 eV laser pulses at an incident fluence of 60 μJ/cm^2 (Fig. 3.3). For this measurement only one of the two beams of the Mach-Zehnder interferometer is used.

In the spectrum two regions are evidenced:

- The first region (Region A), below 1.9 eV kinetic energy, shows a sharp edge that can be well fitted with a Fermi-Dirac function at room temperature. Considering the measured work-function of 4.3±0.1 eV, the edge at about 1.88 eV of kinetic energy is ascribed to a 2-photon photoemission (2PPE) from the Fermi level.
- The second region (Region B), at higher kinetic energies, extends above the 2PPE Fermi edge. The exponential decreasing intensity of electrons photoemitted with

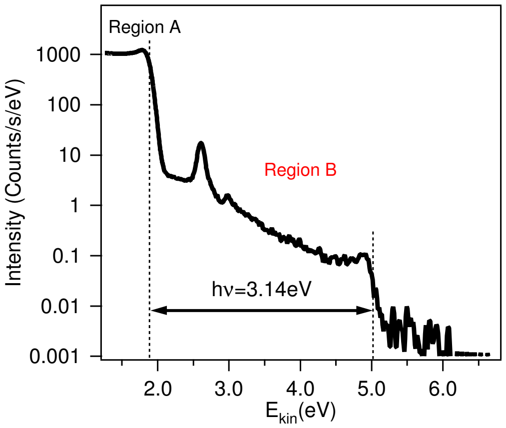

FIGURE 3.3: Photoemission spectrum from Ag(100) obtained at $k_{||}$=0 with 150fs-3.14eV laser pulses with an incident fluence of about 60 μJ/cm^2. The light is *p*-polarized and its angle of incidence is 30° with respect to the surface normal. At about 1.9 eV and at 5 eV, the 2-photon and the 3-photon photoemission Fermi edges are present, whereas the features at about 2.6 eV and 3 eV are ascribed to n=1 and n=2 image potential states, as discussed in Ref. [33]. The energy scale of the spectrum has been aligned on the 2.61eV-IPS peak as explained in section 3.4.1. The data reported in this figure have been smoothed with a binomial algorithm for graphical reasons.

$2h\nu - \Phi < E_{kin} < 3h\nu - \Phi$ has been related to a non-equilibrium electron population created by the absorption of ultrashort laser pulses [33]. The mechanism responsible of the photoemission of the high-energy region will be discussed in the next section. At 5 eV kinetic energy, another sharp feature is visible. This feature is attributed to a 3-photon Fermi edge. To further confirm this assignment we have obtained different evidences (see Ref. [42]): a) the 3-photon Fermi edge is separated by exactly one photon energy from the 2-photon Fermi edge and can be fitted with a Fermi-Dirac function at room temperature; b) total photoemission yield measurements show a quadratic and cubic dependence on laser intensity of Region A and Region B, respectively suggesting a 2-photon and a 3-photon photoemission process involved; c) upon a shift $h\Delta\nu$ of the photon energy, the 3-photon Fermi edge is shifted by $3h\Delta\nu$. The features at about 2.6 eV and 3 eV are ascribed to the first two image potential states as a result of a two-step process: in the first step the IPS are indirectly populated by electrons in the *s-p* bands and in the second step the electrons are photoemitted from IPS via a single-photon photoemission (this mechanism will be described in detail in the next chapter).

We stress the fact that experimental parameters (size of the laser spot, laser intensity) have to be carefully chosen to maximize the intensity of the impinging laser field, in order to evidence non-linear effects, and the count rate of the photoemitted electrons, in order to acquire spectra in a reasonable time. On the contrary it is necessary to minimize space-charge effects, due to a high rate of photoemitted electrons, which result in a deformation or shifting of the photoemission spectrum. The best compromise is found by tailoring the experimental parameters in order to have an energy shifting of the spectrum smaller than 200 meV, but, at the same time, a laser intensity sufficient to evidence a ratio between the intensity of the 3-photon and 2-photon Fermi edges of about 10^{-4}-10^{-5}. In the spectrum in Fig. 3.3, the n=1 IPS kinetic energy has been taken as a reference for the energy scale. In fact, if E_{bin} is the binding energy of the first IPS and $h\nu$ is the photon energy, the electrons are photoemitted from this state with a kinetic energy $E_{kin} = h\nu - E_{bin}$. In the case of n=1 IPS on Ag(100) we obtain E_{kin}=(3.14-0.53) eV=2.61 eV [13, 18]. By using this procedure, the binding energies of the spectral features reported in Fig. 3.3, are not affected by the 200 meV-energy shift due to space charge effects.

3.4.2 Scattering-mediated transitions as origin of $\mathbf{k}_{\parallel}$ exchange

In this section we discuss the physical mechanism at the origin of the high-energy region (Region B) of the spectrum reported in Fig. 3.3. In the following, we will schematize multiphoton transitions in terms of three different categories [43]:

- *Coherent Transitions*: when the intermediate state is a virtual state.
- *Direct Transitions*: when the intermediate state is a real state and there is no change of the electron momentum parallel to the surface sample. These transitions can also be referred to as *resonant transitions.*

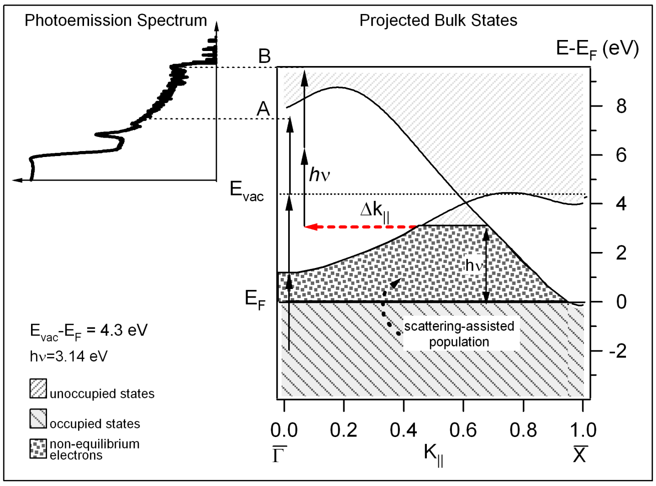

FIGURE 3.4: On the right: the projected band structure along the $\bar{\Gamma}\bar{X}$ direction of Ag(100) surface Brillouin zone is shown (taken from Ref. [9]). Two possible photon absorption mechanisms are shown. Mechanism A is a one photon resonant-three photon photoemission. Mechanism B involves an exchanging-momentum electron-ion collision. E_{vac} is the vacuum level and E_F is the Fermi level. On the left: photoemission spectrum on Ag(100), acquired with 3.14eV-150fs laser pulses, at $k_{||}=0$ (the spectrum is taken from Fig. 3.3).

- *Indirect Transitions*: when the intermediate state is a real state and the electron momentum parallel to the sample surface is varied during the transition from initial to final state.

The mechanism to explain the origin of the high-energy electron tail is an *indirect* 3-photon photoemission (3PPE) process. We exclude a 3PPE coherent process, because i) in Fig. 1 a flat distribution above the 2PPE Fermi edge, reproducing a constant density of occupied states in Ag (the $\sqrt{E}$ dependance does not affect the argumentation), is expected rather than an exponential decreasing one. Moreover, ii) in Ref. [42] the ratio between the probability of a 2nd- and 3rd- order photoemission from the Fermi edge is estimated, through a perturbative calculation, to be 10^{-6}. On the contrary the ratio between the first part of the high-energy region ($E \simeq 2.2$ eV) and the 2-photon Fermi edge, reported in the the spectrum in Fig. 3.3, is about 10^{-2}.

We also exclude a direct 3PPE, where the first photon creates a free-electron population in the empty states above the Fermi level and upon two photon absorption these electrons are photoemitted without a $k_{\|}$-momentum exchange. If both the absorption and photoemission processes took place along $k_{\|}=0$, the photoemission intensity of the electron gas should show a cut-off at about 1.2 eV above the 2-photon Fermi-edge (Fig. 3.4, mechanism *A*), i.e. at the end of the available bulk states. On the contrary the high-energy electron tail monotonically decreases well above this energy, as shown in Fig. 3.4. Therefore a plausible mechanism is an indirect three photon process mediated by scattering events which change the $k_{\|}$-momentum of the photoemitted electrons. In this picture the scattering-mediated photon absorption creates a non-equilibrium electron population in the unoccupied bulk states at $k_{\|} \neq 0$, where available states extend up to the vacuum level. A scattering event is also responsible for the electron $k_{\|}$-momentum exchange necessary to the photoemission process at $k_{\|}=0$ (Fig. 3.4, mechanism *B*).

These conclusions are strengthened by two recent theoretical works, where the photoexcited electron dynamics in metals is studied [34, 35]. In particular the authors investigate the interaction of the laser field with the conduction electrons in metals. In fact a direct resonant dipole transition between two levels in the conduction *s-p* band is forbidden by energy and momentum conservation. The problem is solved by attributing the absorption mechanism to a scattering-mediated process: i) photon absorption during electron collisions with phonons [34] or ii) inverse bremsstrahlung process [35]. Along this line we attribute the scattering mechanism responsible for the electron $k_{\|}$-momentum exchange to an electron-phonon collision, which, during the n-photon absorption, changes only the $k_{\|}$ momentum and not the energy of the electrons. It is worth noting that the step-like function observed in our experiment (Fig. 3.3), where the electron distribution decreases below the Fermi edges separated in steps of $\hbar\omega$, is also qualitatively reproduced in the calculations on Al, see Ref. [35].

3.4.3 Non-equilibrium electron dynamics probed by time-resolved photoemission spectroscopy

As a consequence of the delineated physical frame, the collected photoemission spectrum constitutes a snapshot, within the laser pulse duration (150 fs), of the non-equilibrium electron distribution in the empty *s-p* bands at $k_{||}$ different from zero. For this reason pump-probe measurements of the high energy electron tail constitute a tool for investigating the non-equilibrium dynamics of electrons excited in the conduction band. In this section we report on direct measurements of the lifetime of the non-equilibrium electron population.

To investigate the non-equilibrium electron dynamics, pump-probe measurements have been carried out in Region A ($1.66 \leq E \leq 1.88$) and Region B ($2.18 \leq E \leq 4.18$) of the spectrum reported in Fig. 3.3. Both pump and probe are 3.14eV-150fs pulses. The laser intensity I_0 is monitored during the acquisition of spectra at different delays Δt. In order to take into account possible drifts of the laser fluence, the photoemitted integrated intensity of a n-order non-linearity region has to be divided for the nth power of the mean value of the laser intensity. For this reason it is important to exactly evaluate the non-linearity order of the regions A and B. In the inset of Fig. 3.5 the photoemission integrated intensities are plotted versus the laser fluence. The integrated intensity of the Fermi edge region (in the 1.66-1.88 eV energy range) increases as I^2 with the laser fluence. This result confirms the interpretation as a 2-photon photoemission mechanism. The intensity of the high-energy electron tail, obtained by integrating the 0.3-2.3 eV energy range above the 2-photon Fermi edge, and subtracting the contribution of n=1 and n=2 IPS, scales as I^3, in agreement with the result reported in Ref. [42] and compatible with an interpretation in terms of an *indirect* 3-photon photoemission process. As a consequence, the integrated intensity of the 2-photon Fermi-edge region is normalized to I_0^2, whereas the yield of the second region is divided by I_0^3, to avoid the influence of the laser intensity drift on the photoemission intensity.

In Fig. 3.5 the autocorrelation of the normalized integrated charge of the two regions is shown. The ratio between the measured intensity of the Fermi-edge region (black squares) at Δt=0 and at Δt=300 fs is 2, confirming a second order process, and the FWHM of the

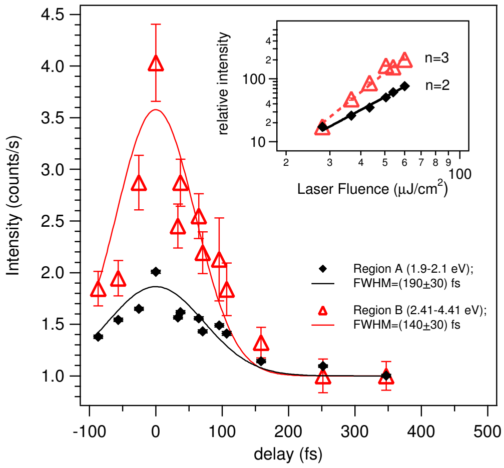

FIGURE 3.5: The photoemission integrated intensities are plotted versus the delay time between the pump and the probe pulses. The pump and probe measurements are carried out at normal incidence and at an angle of 30° between the detector and the normal to the sample surface. In the inset the integrated intensities of the Fermi (black squares) and high-energy electron (red triangles) regions are plotted versus the laser fluence. To estimate the non linearity order (n), the data are fitted with a power function.

gaussian fit of the autocorrelation is 190±30 fs. Concerning the high-energy electron region (red triangles), the peak/background ratio of about 4 is in agreement with the assignment of a third order photoemission process, whereas the FWHM of the autocorrelation is 140±30 fs.

If we consider a second- and third-order autocorrelation of a laser pulse with a gaussian temporal profile of 150 fs, we obtain a value for the FWHM of 210 fs and 170 fs, respectively. These values are compatible, within the experimental error, with the measured ones (see Fig. 3.5), indicating that no broadening of the autocorrelation is detectable within the experimental resolution of 150 fs. The conclusion is that the relaxation time of the high-energy electrons is faster than 150 fs.

The measured mean relaxation time $\langle\tau\rangle$ for electrons in the Region B ($0.3<(E\text{-}E_F)$

<2.3 eV), indicates that the thermalization of the non-equilibrium population is rapidly reached via electron-electron scattering. To estimate the relaxation time of the electron gas, it is possible to apply the Fermi liquid theory under the random-phase approximation (RPA), according to the equation [36]:

$$\tau_{e-e} = \tau_0 \left[\frac{E_F}{(E - E_F)} \right]^2 \tag{3.2}$$

where (E_F) is the Fermi energy and ($E - E_F$) is the electron energy relative to the Fermi level. The proportionality constant τ_0 can be calculated using the Lindhard dielectric function:

$$\tau_0 = \frac{128}{\pi^2 \sqrt{3}} \frac{1}{\omega_p} \tag{3.3}$$

and ω_p is the plasma frequency, given by the expression $\omega_p = (4\pi n e^2)/m$ with n the electron density and m the electron mass. It is possible to use this scaling law in the limit $(E - E_F) \gg KT$, where KT is the Boltzmann temperature. In our case $(E - E_F) > 0.3$ eV, whereas KT is of the order of 26 meV at room temperature.

To compare the measured lifetime of the non-equilibrium electron population with the value predicted by Fermi-liquid theory, it is necessary to calculate the mean lifetime $\langle \tau \rangle$ of a flat electron distribution in the conduction band, under the hypothesis that at t=0 the laser-induced occupation of the states above the Fermi level is constant. The mean lifetime is given by the expression:

$$\langle \tau \rangle = \frac{1}{N} \int_{n(E_1)}^{n(E_2)} \tau(E) dn(E) \tag{3.4}$$

where $dn(E)$ is the number of electrons of energy between E and $E + dE$, N is the total number of electrons, E_1 and E_2 are the energy integration limits.

By taking into account that, in a parabolic band, $dn(E) = a\sqrt{E} dE$, where a is a constant, we obtain:

$$\langle \tau \rangle = \left[\int_{E_1}^{E_2} a\sqrt{E} dE \right]^{-1} \cdot \int_{E_1}^{E_2} \tau_0 \left[\frac{E_F}{(E - E_F)} \right]^2 a\sqrt{E} dE \tag{3.5}$$

Substituting the values E_F=5.49 eV [44], ω_p=8.98 eV [44], E_1=E_F+0.3 eV=5.79 eV and E_2=E_F+2.3 eV=7.79 eV, the mean lifetime results to be about 23 fs, a value compatible

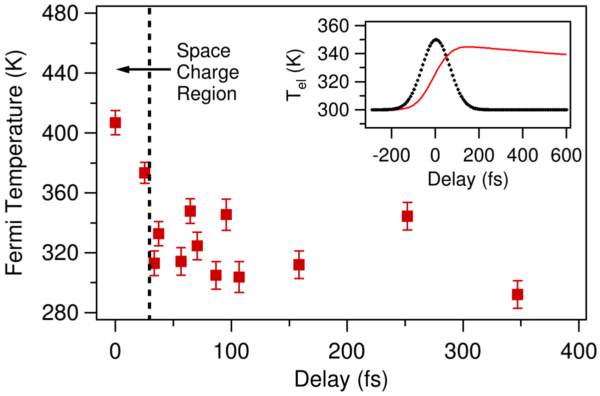

FIGURE 3.6: The Fermi temperature, estimated by fitting the 2PPE Fermi edge with a Fermi-Dirac function convoluted with a gaussian, is shown for different delay times. In the inset the time evolution of the electron temperature (red line), estimated by the two-temperature model, and the pulse temporal profile (black dots) are shown. When the pump and probe pulses overlap in the time-domain (Δt<30 fs), the high photoemission intensity results in a slight deformation of the Fermi edge.

with the measured one ($\langle\tau\rangle < 150$ fs). This result indicates that, within the pulse duration, the laser electric field coexists with a non-equilibrium electron gas which is thermalizing through electron-electron scattering on the same timescale.

3.4.4 Energy exchange between equilibrium and non-equilibrium electron distributions

As discussed in Section 3.2, previous experiments [39, 40] investigating the non-equilibrium electron dynamics on metals, were performed with an incident intensity of the pump beam of about 1 GW/cm^2. On the contrary we used a very low incident laser intensity (I$\simeq$0.1 GW/cm^2). For this reason, in our case, the energy absorbed by the non-equilibrium electron distribution is not sufficient to significantly heat the Fermi-Dirac bulk electron distribution.

This can be proved by measuring the temperature increase of the 2PPE Fermi distribution, due to energy exchange between the excited-electrons and bulk-electrons, in analogy with Ref. [39, 40]. In Fig. 3.6 the temperature estimated by fitting the 2-photon Fermi edge with a Fermi-Dirac function convoluted with a gaussian which takes into account the apparatus resolution, is plotted versus the delay time between pump and probe pulses. To perform these measurements it is important to avoid any deformation due to space-charge effects, that could introduce errors in the fitting of the Fermi edge. For this reason the laser intensity has to be tailored in order to reduce space-charge deformations but, at the same time, to assure a sufficient photoemission intensity of the high-energy region. The best compromise is to tolerate a modest space-charge effect when the pump and probe pulses are coincident in the time domain (Δt=0) and the photoemitted intensity is twice with respect to the intensity at a delay greater than the laser pulse duration (Δt>150 fs). For this reason the Fermi temperature heating measured at Δt=0 (T=410 K) and Δt=30 fs (T=370 K), is attributed to a slight deformation of the spectrum due to a high photoemission intensity. This statement is confirmed by the fact that Δt=30 fs is a timescale too short for any energy exchange between the electron system and the phonon gas. On the contrary the heating of the equilibrium electron distribution appears after the laser pulse duration, where the mean Fermi temperature is about 320 K.

At this light, we have estimated the heating of the Fermi temperature by using the two temperature model [37, 38], i.e. supposing that the energy absorbed from the non-equilibrium electron gas is totally transferred to the equilibrium Fermi distribution, before that any energy exchange with the lattice could take place. It has been recently demonstrated that, during laser irradiation, the energy exchange between electrons and lattice starts before thermalization of non-equilibrium electrons is completed [39, 40, 45, 46, 47, 48, 49]. As a consequence, this model gives an upper bound for the Fermi temperature heating. The time evolution of the electron temperature is given by the coupled equations [37, 38]:

$$\begin{aligned} C_e(T_e)\frac{\partial T_e}{\partial t} &= -G\cdot(T_e - T_l) + P(t) \\ C_l(T_l)\frac{\partial T_l}{\partial t} &= G\cdot(T_e - T_l) \end{aligned} \tag{3.6}$$

where T_e and T_l are the electron and the lattice temperatures, P(t) is the laser intensity profile. The values used are the laser fluence (20 μJ/cm^2), the reflectivity (for Ag

r=0.86% [50] at about 0°), the penetration depth (16 nm) [50], a pulse width of 150 fs, heat capacity (γ=96 J/m^{3}K^2) [51], and the phonon-electron coupling constant G=10^{16} W/m^{3}K [51]. The calculated temperature behavior is reported in the inset of Fig. 5. The Fermi temperature after the laser pulse, is about 345 K. This value is compatible with the slightly smaller experimental result (T≃320 K), considering that in the pump-probe experiment, the photoemission spectrum is a convolution between an electron distribution at room temperature due to the pump pulse and a second distribution at higher temperature probed by the second pulse. This result confirms that the non-equilibrium electron population created by a laser pulse at very low laser intensities (I≃0.1 GW/cm^2) on an Ag single crystal, perturbs in a negligible way the equilibrium bulk electron system, which behaves as a thermal bath.

3.4.5 Above threshold photoemission

It is important to underline that the 3-photon Fermi edge shown in Fig. 3.3 and attributed to an *indirect* 3-photon photoemission (see Fig. 3.4) is due to an "Above-Threshold Photoemission" (ATP) process, because, upon the absorption of two photons, the electrons at the Fermi level should be already free.

The ATP process is the counterpart in solids of the widely studied "Above-Threshold Ionization" on atoms [52, 53, 54, 55, 56]. ATI is the process by which an atom, subject to an intense electromagnetic field of frequency ν, is ionized by the absorption of a number of photons that exceeds the minimum number strictly necessary to overcome the ionization potential W_{ion}. In literature only a few studies do claim observations of ATP in solids [57, 28, 58], but none of them shows spectra were an above-threshold multiphoton replica of a spectral feature is clearly visible and unambiguously identified (for a detailed discussion see Ref. [42]).

In atoms, ATI spectra generally consist of several peaks of increasing order and the intensity ratios between successive emissions are comparable [53]. On the contrary, in our case, we observe only one spectral feature photoemitted *above-threshold* with an intensity four order of magnitude lower as compared to the emission of second order (see Fig. 3.3). For the above mentioned reason a direct dipole-transition process cannot be, a-priori, ruled out as the mechanism responsible for the process. We made an estimate to investigate such possibility. The differential cross-section for an n-photon absorption involving the initial and final states $|i\rangle$ and $|f\rangle$ is, writing the interaction hamiltonian in the *velocity gauge*,

$$\frac{dW_{i\to f}^{(n)}(\mathbf{k}_f)}{d\Omega}=\frac{2\pi}{\hbar^2}\left(\frac{e^2}{2m^2c\epsilon_0}\frac{I}{\omega^2}\right)^n\left|T_{i\to f}^{(n)}(\mathbf{k}_f)\right|^2\rho\left(E_{k_f}\right), \tag{3.7}$$

where ϵ_0 is the electric permittivity, e the electron charge, $\rho\left(E_{k_f}\right)$ the free electron final density of states evaluated at the photoemitted electron energy $E_{k_f}=nh\nu-\ \Phi$, $\mathbf{k_f}$ being the wave vector of the electron in the final state, whose modulus is determined from energy conservation $\hbar^2k_f^2/2m=n\hbar\omega-\Phi$. I is the *absorbed* laser intensity. The transition matrix element remains defined as

$$T_{i\to f}^{(n)}\equiv\left\langle f\left|p\underbrace{G\left(E_i+(n-1)\hbar\omega\right)p}_{n-1\ such\ terms}...G\left(E_i+\hbar\omega\right)p\right|i\right\rangle \tag{3.8}$$

with $p=\epsilon\cdot\mathbf{p}$, ϵ being the polarization unit vector of the e.m field $\mathbf{E}$, $\mathbf{p}$ the momentum operator and $G\left(E_i+m\hbar\omega\right)$ the propagator of the unperturbed hamiltonian after absorption of the m^{th} photon. The eigenvalues E_i and the corresponding eigenvectors, entering the perturbative calculation, are the solutions of the unperturbed semi-infinite crystal hamiltonian. We pinpoint that the above threshold transition involves the mixing of the final free electron state with *all* the unperturbed hamiltonian eigenstates and not only with the eigenstates entering the continuum spectrum, that would give null matrix elements. A rough estimate for the ratio $\partial_\Omega W_{i\to f}^{(3)}(\mathbf{k}_f)/\partial_\Omega W_{i\to f}^{(2)}(\mathbf{k}_f)$, among the 3-photon and the 2-photon differential cross-sections, is $\sim 10^{-6}$. The calculation was carried out neglecting the details of the matrix elements, within the same approximations used in [59]:

$$\frac{T_{i\to f}^{(3)}(\mathbf{k}_f)}{T_{i\to f}^{(2)}(\mathbf{k}_f)}\approx\sum_j\frac{p}{(E_i-E_j)+2\hbar\omega}, \tag{3.9}$$

$p\sim\hbar k_f=\sqrt{2m(3\hbar\omega-\Phi)}$. Assuming that only one particular eigenvalue $E_j=\tilde{E}$ is relevant in the sum, the right term in Eq. 3.9 reduces to $p/\left(\Delta E+2\hbar\omega\right)$, where $\Delta E\equiv E_i-\tilde{E}$. We focused on the values of ΔE that fall in the interval $[-1.2,0]$ eV and $[-3.8,-4.3]$ eV, the former range meaning that the prevailing unperturbed eigenstates contributing to the transition matrix are the unoccupied s-p bulk states laying 1.2 eV above the Fermi level (see Fig. 3.4), the latter privileges image-states lying below the vacuum level (refer to Fig. 3.4). We note that it never occurs $\Delta E + 2\hbar\omega = 0$, being the emission process *non*-resonant. The present estimate for the ratio, 10^{-6}, is to be compared with the experimental ratio of the photoemission intensity of the 3-photon and 2-photon Fermi edges, reported in Fig. 3.3, of 10^{-4}. The confrontation shows an experimental value two order of magnitude higher than expected.

In the above calculation we have neglected the possibility of scattering-mediated light absorption, but we have shown, in section 3.4.2, that such processes of photon absorption during electron-phonon collisions [34], are a plausible mechanism to explain the photoemission spectrum reported in Fig. 3.3. A theory of Above-Threshold Photoemission that takes into account scattering-mediated transitions is not available at the moment. In any case we believe our results constitute an important bench mark for future theoretical works on scattering-mediated photoemission processes in metals under moderate intensity radiation field.

3.5 Summary

Time-resolved non-linear photoemission is carried out on Ag(100). The high kinetic energy electron tail detected in the photoemission spectra is attributed to a non-equilibrium free-electron gas. We report on the evidence that these electrons are emitted by a 3-photon photoemission process mediated by a $k_{\parallel}$-exchanging scattering mechanism. Our results can be interpreted at the light of recent theoretical models [34, 35] in which the scattering mechanism is attributed to an electron-phonon collision during the photon absorption or to an inverse bremsstrahlung process. These results clarify the question about the energy and momentum conservation during the photon absorption process.

Time-resolved measurements show that, at very low laser intensities (I$\simeq$0.1 GW/cm^2), the relaxation dynamics of the non-equilibrium electrons (τ <150 fs) is in agreement with the Fermi-liquid theory. The heating of the Fermi edge, detected after laser irradiation, can be neglected. This result confirms that, in this regime, the non-equilibrium electron distribution weakly perturbs the equilibrium bulk distribution.

Chapter 4

Image Potential States as a Probe of Non-Equilibrium Electron Population

Image Potential States (IPS) constitute a unique tool to investigate the properties of a 2-dimensional electron gas at a metallic surface. The study of IPS in the non-equilibrium regime gives information on the interaction with the 3-dimensional electron gas, induced in the bulk states by excitation with ultrashort pulses.

Angle-resolved non-linear photoemission spectroscopy is performed on Ag(100). The violation of the electric dipole selection rules, normally respected in the excitation and photoemission process from IPS, is demonstrated and attributed to an indirect population mechanism. The measured decrease of the IPS effective mass, with respect to the non-interacting case, is interpreted as the fingerprint of the many-body interaction between electrons on IPS and the photoexcited electron population in the conduction band. These results call for a further theoretical investigation concerning the role of the non-equilibrium electron distribution in the many-body interaction potential.

4.1 Introduction

Image potential States have been widely investigated from a theoretical point of view, because they constitute a simple model of a 2-dimensional electron gas, interacting with the bulk electron distribution. Current many-body theories approach the problem by calculating the irreducible self-energy ($\Sigma^*(\mathbf{k},\omega)$, where $\mathbf{p}=\hbar\mathbf{k}$ and $E=\hbar\omega$ are the quasi-particle momentum and energy) of an electron at the metal-vacuum interface. The self-energy acts as a renormalization of the quasi-particle excitation spectrum, taking into account that the electron is subjected to interactions. Self-energy calculations are, in general, quite involved. The GW approximation [60], i.e. vertex diagrams in the perturbative expansion of the interaction potential W are neglected, is commonly adopted to simplify the problem. In this case the electron irreducible self-energy is simply related to the "dressed" potential $W(\mathbf{k},\omega)$, that incorporates the many-body effects:

$$\Sigma^*(k,\omega) = i\int \frac{d\mathbf{q}}{(2\pi)^3}\int \frac{d\omega'}{2\pi} W(\mathbf{q},\omega')G(\mathbf{k}-\mathbf{q},\omega-\omega') \tag{4.1}$$

where $\hbar\mathbf{q}$ and $\hbar\omega'$ are the exchanged momentum and energy and $G(\mathbf{k},\omega)$ is the electron Green function, given by the Dyson equation form:

$$G(\mathbf{k},\omega) = \frac{1}{\omega - \epsilon_k^{(0)} - \Sigma^*(\mathbf{k},\omega)} \tag{4.2}$$

where $\hbar\epsilon_k^{(0)}=\hbar^2\mathbf{k}^2/2m$ is the unperturbed electron energy spectrum. In this framework the damping rate Γ is related to the imaginary part of the irreducible self-energy Σ^* and so it is straightforward to obtain the electron lifetime τ as the inverse of Γ. From Eq. 4.1 it is evident that an accurate knowledge of the potential W is needed in order to perform self-energy calculations and electron lifetimes estimations. For this reason the comparison of the calculated lifetimes with the experimental values constitutes a benchmark for many-body theories and a verification of the knowledge of scattering mechanisms at a metal surface [4].

So far the electron dynamics of IPS has been experimentally studied mainly by multiphoton photoemission induced by a sequence of *direct* electronic transitions from the initial state to the final state (see Chapter 2), i.e. the IPS states constitute a resonance for the non-linear photoemission process. In this section we present a different and new approach to the problem. We demonstrate, in fact, that, exciting Ag(100) with 3.14eV-150fs laser pulses, it is possible to indirectly populate IPS, through scattering-mediated transition processes. In addition IPS are found to co-exist with a high density ($n \approx 10^{19}$-10^{20} electrons/cm^3) non-equilibrium electron population in the conduction band. As a consequence of the interaction of IPS electrons with the excited bulk electron distribution, the value of the IPS effective mass ($m^*/m \simeq$0.88) is measured to decrease, as compared to the non-interacting case ($m^*/m \simeq$1, see Chapter 2).

Our results open the possibility of studying population of empty surface states via scattering-assisted processes and, in particular, call for a further theoretical investigation to understand how the non-equilibrium electron population influences the "screened" potential W, necessary for the calculations of IPS electron lifetimes and effective masses.

4.2 Direct *vs* indirect population of IPS

IPS properties are generally investigated through non-linear photoemission spectroscopy. In particular, as shown in Chapter 2, two-photon photoemission is performed on Ag(100), with a photon energy ($\hbar\nu$ = 4.28 eV) greater than the energy difference between the IPS and the Fermi level, in order to directly populate IPS from occupied bulk states. In this case a value near unity for the effective masses is measured, in agreement with theoretical predictions based on the hypothesis that IPS can be schematized as a 2-dimensional electron gas at the metal surface [12, 19, 9]. Moreover the lifetimes obtained through time-resolved photoemission [22] or inverse-linewidth measurements [18] are compatible with recent many-body calculations [24]. No influence of the laser-induced non-equilibrium population and of indirect population mechanisms is reported with this excitation scheme. These findings are consistent with the fact that, exciting the Ag with photons at 4.28 eV, direct *interband* transitions from the Ag 4d bands to the bands above the Fermi level (see Fig. 4.1) results in a strong dipole-allowed linear optical absorption. This excitation channel accounts for $\sim$ 90% of the absorbed intensity [61, 62], preventing the formation of a high-density hot-electron population.

On the contrary, such a strong linear *interband* absorption is not possible with 3.14 eV photons and bulk *intraband* photoabsorption creates the non-equilibrium electron gas in

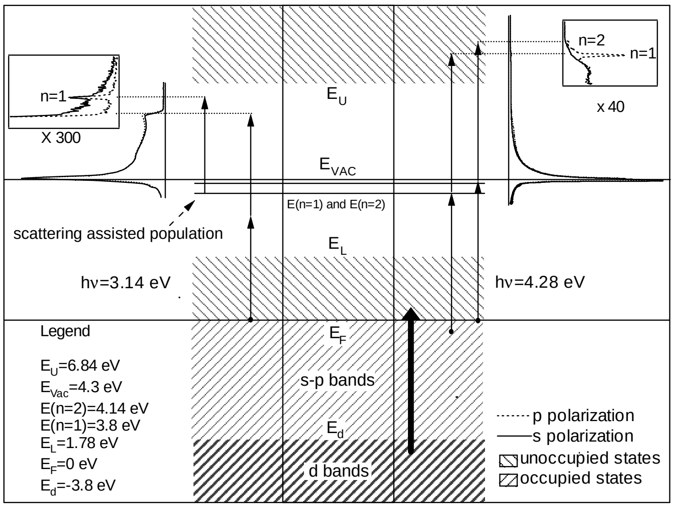

FIGURE 4.1: Energy-level diagram for Ag(100) at $k_{\|} = 0$. A representation of the photoemission processes induced at a photon energy of 3.14 eV (on the left) and 4.28 eV (on the right) is shown. The values reported in the legend are from Ref. [12]. E$_U$ and E$_L$ represent the upper and lower bound of the energetic gap in the projected bulk bands on the surface. E(n=1) and E(n=2) are the energy levels of the first two image potential states.

the empty states of the conduction band. The scattering mechanism responsible for the energy and momentum conservation in the transition between two levels in the *s*-*p* bands is discussed in detail in Section 3.4.2 of Capter 3. In Fig. 4.1 the spectra measured at $h\nu$ = 3.14 eV and $h\nu$ = 4.28 eV, represented on a linear scale, are shown for both *s*- and *p*-polarization. The prominent features in these spectra are the emission peaks near zero kinetic energy, i.e. those originating from the indirect secondary electron emission [63]. However, at $h\nu$=3.14 eV the zero-energy peak vs Fermi edge ratio is lower with respect to that measured at $h\nu$=4.28 eV. This confirms the role of the direct interband absorption from the *d* bands at 4.28 eV, that populate the available states near the Fermi level, giving an additional contribution to the zero-energy peak emission intensity via one-photon photoemission.

To substantiate in a more quantitative way this picture, we can estimate the density of the non-equilibrium electron population excited in the conduction band in the two cases. The density of absorbed energy ε_{abs} is given by:

$$\varepsilon_{abs} = \frac{\alpha F_{inc}}{L} \tag{4.3}$$

where F_{inc} is the incident fluence, α is the absorption coefficient and L is the penetration depth. In the case of resonant excitation we can substitute in eq. 4.3 the values of the parameters relative to the wavelenght λ=289 nm: $^1F_{inc}$=0.03 mJ/cm^2, α=0.82 (@ p-polarized light at 30° of incident angle); L=20 nm [50]. The result is that the density of absorbed photons is about $2{\cdot}10^{19}$cm^{-3}. Considering that the 90% of the absorbed intensity results in the dipole allowed $4d \rightarrow 5s$ transition, only about $2{\cdot}10^{18}$electrons/cm^3 are excited in the conduction band. On the contrary, for the non-resonant excitation scheme (λ=790 nm), we have: $^1F_{inc}$=0.3 mJ/cm^2, α=0.18 (@ p-polarized light at 30° of incident angle); L=17 nm [50] and the calculated density of photons is about 10^{20}cm^{-3}. In this case, under the hypothesis that all the energy is absorbed through *intraband* transitions, the estimated density of electrons in the s band is n_{neq}=10^{20}electrons/cm^3 a value about 2 order of magnitude greater with respect to the previous case. It is important to underline that the density of electrons in the s-p bands is about $n_s \simeq 6{\cdot}10^{22}$electrons/cm^3, so that the density of the non-equilibrium population is not negligible ($n_{neq}/n_s \simeq 2{\cdot}10^{-3}$).

4.3 Experimental set-up

In this section we report on a schematic description of the experimental set-up. The light source is an amplified Ti:Sapphire laser, emitting 800nm-150fs pulses at 1 kHz of repetition rate. The pump-probe experiment is performed with a photon energy hν=3.14 eV, obtained by duplicating the fundamental radiation with a BBO crystal.

The Ag single-crystal, oriented along the (100) surface, is kept in a μ-metal ultra-high vacuum chamber with a base pressure of 2x10^{-10} mbar at room temperature. The sample

---

[1] The values of F_{inc} are representative of the typical laser intensities used in the two different excitation schemes.

surface is cleaned and monitored with the procedures described in Section 2.4 of Chapter 2. The measured work function is 4.3±0.1 eV.

The kinetic energy of the photoemitted electrons is measured by the high resolution time of flight (TOF) spectrometer (see Appendix A), characterized by an acceptance angle of $\pm 0.83^\circ$. The total energy resolution of the experimental set-up (laser linewidth + detector resolution) is 35 meV at a kinetic energy of 2 eV.

For further details, see Sec. 2.4 of Chap. 2 and Sec. 3.3 of Chap. 3.

4.4 Results

4.4.1 Violation of the electric dipole selection rules

Image Potential States on Ag(100) are investigated through angle-resolved non-linear photoemission. The sample is excited with linearly polarized, 150 fs pulses at $h\nu$=4.28 eV and $h\nu$=3.14 eV, in s polarization (electric field perpendicular to the plane of incidence) and p polarization (electric field parallel to the plane of incidence). The angle of incidence is 30° with respect to the surface normal. Since the dipole moment of the IPS is perpendicular to the surface, the probability of excitation with s-polarized light in the dipole approximation is zero [17, 62].

For the direct photoemission process at $h\nu$=4.28 eV, a result consistent with the polarization selection rules for IPS is found, as shown in Fig. 4.2A. This result is in agreement with the large body of existing literature, where direct excitation is used [17, 62, 58] and it is a clear indication that the experimental data are free of possible artifacts. The negligible secondary electron background observed in these spectra for kinetic energies larger than 4.5 eV, leads to the well-known conclusion that only a photon-induced direct population mechanism is responsible for IPS emission, whereas electron scattering plays a negligible role in these processes.

The detection of the IPS populated at $h\nu$=3.14 eV is significantly more difficult and requires an electron spectrometer with a very high signal to noise ratio. In the present experiment the noise in the detection apparatus (i.e. counts without laser excitation) is negligible (less than 10^{-4} counts/s). These spectra are presented in Fig. 4.2B. The

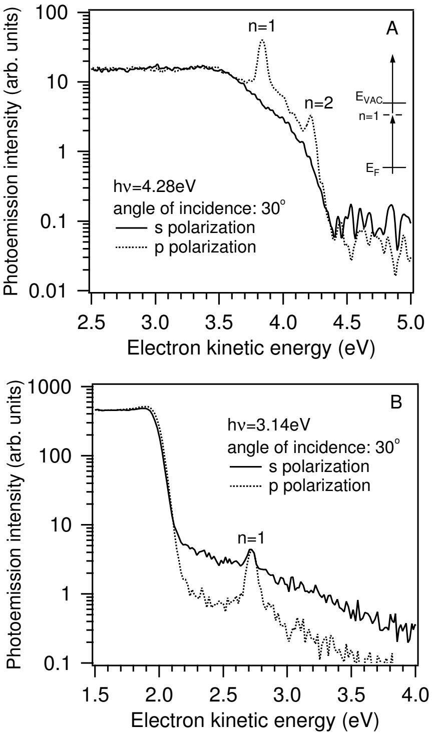

FIGURE 4.2: Multi-photon photoemission spectra from Ag(100) obtained with 150 fs laser pulses at an angle of incidence of 30° with respect to the surface normal. A) Photoemission spectra at $h\nu = 4.28$ eV in s and p polarization. The inset represent a schematic energy level diagram at $k_{\|} = 0$ of Ag(100) surface states, showing a direct one-photon population, two-photon photoemission via the n=1 IPS. B) Photoemission spectra at $h\nu = 3.14$ eV in s and p polarization. A two-photon population is forbidden by dipole selection rules in s polarization.

sharp edge observed at about 2 eV kinetic energy can be unambiguously assigned to the Ag(100) Fermi edge resulting from a 2PPE absorption process (see Chap. 3). A distinct spectral feature is detected at 2.76 eV kinetic energy. Its intensity is two decades smaller than the emission at the Fermi edge, while its binding energy (E_{bin}), determined from work function measurements, is 500±100 meV, in agreement with the E_{bin} of n=1 IPS [17, 18]. In addiction, the peak of this feature shifts with photon energy by an equal amount. Therefore, it is assigned to a single-photon photoemission from the n=1 IPS. Interestingly, this feature sits on a high-energy electron background, which is attributed to the laser-induced non-equilibrium population in the *s*-*p* bands, as discussed in Chap. 3.

Rather surprisingly, this spectral feature is still observable with *s*-polarized light. This is at variance with measurement using a photon energy of 4.28 eV (see Fig. 4.2A), where a total quenching of the IPS electron intensity is observed in *s* polarization. These findings imply that the polarization selection rules, for the population and/or photoemission from IPS, are violated in *s* polarization photoemission at $h\nu$=3.14 eV.

4.4.2 Dependance on light polarization

In Fig. 4.2B the photoemission spectra collected with *p*- and *s*-polarized light at an incident angle of 30° and with an incident fluence of 55 μJ/cm^2 and 85 μJ/cm^2, respectively, are shown. A dependence of the high-energy region ($2.2 < E < 5.4$ eV) on light polarization is evident. The ratio between the integrated intensity of the electron tail for the two polarizations is about 0.22.

It is important to evaluate if this value simply reflects the variation of the absorbed laser fluences in *s* and *p* polarization. To take into account this influence, the non-linearity order of the different energy regions of the spectrum has to be considered. In Chapter 3, we have demonstrated that a third-order process is involved in the photoemission of the high-energy electron tail. If we evaluate, by taking into account Fresnel equations, the ratio I_p^3/I_s^3, where I_p and I_s are, respectively, the absorbed intensities for *p*- and *s*- polarizations, we obtain a value of about 0.77, different from the measured one. This discrepancy suggests that the electron tail intensity does not simply depend on the absorbed fluence, but an important role is played by the direction of the electric field vector incident on the sample

TABLE 4.1: Measured and calculated electron effective mass (in free electron mass units m*/m) for the n=1 image potential state on Ag(100)

direct population	calculated	indirect population
1.6 ± 0.3^a	0.95^b	0.88 ± 0.01^c
1.2 ± 0.2^d	1.03^e	0.88 ± 0.04^f
1.15 ± 0.1^b	1.0^g	
0.99 ± 0.02^h		
0.97 ± 0.02^i		

a)Reference [8]
b)Reference [13]
c)This work, *p* polarization, measured along $\bar{\Gamma}\bar{X}$.
d)Reference [7]
e)Reference [12]
f)This work, *s* polarization, measured along $\bar{\Gamma}\bar{X}$.
g)Reference [9]
h)Reference [18], measured along $\bar{\Gamma}\bar{M}$.
i)Reference [18], measured along $\bar{\Gamma}\bar{X}$.

---

surface.

4.4.3 Electron effective mass

Angle-resolved multi-photon photoemission measurements are performed on Ag(100), with 3.14eV-150fs laser pulses, in *s* and *p* polarization schemes. These photoemission spectra are reported in Fig. 4.3 and 4.4, where the dispersion of the IPS peak is shown. A parabolic dependence of the electron kinetic energy on parallel momentum is clearly detected.

The effective mass measurements are reported in Fig. 4.3b and 4.4b. The effective mass $m^* = \hbar^2/(d^2E/dk_{\|}^2)$, associated with the electrons in the first image potential state, is measured by a parabolic fitting of the energy versus wave-vector position of the IPS peaks

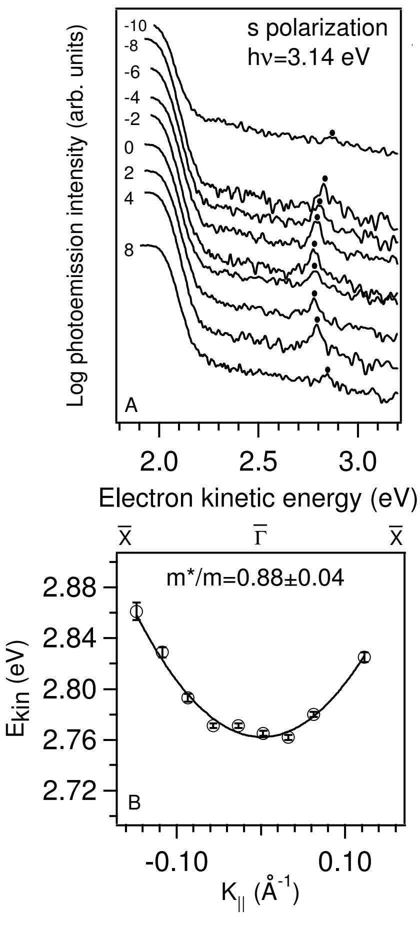

FIGURE 4.3: Multi-photon photoemission spectra from Ag(100) obtained with 150 fs, *s*-polarized laser pulses at an angle of incidence of 30° with respect to the surface normal. A) Angular dispersion of the spectral feature appearing on the high-energy electron tail along the $\bar{\Gamma}\bar{X}$ direction of the surface Brillouin zone. Each spectrum is labelled with the detection angle between the TOF axis and the surface normal. The center of each feature is indicated with a dot as a guide to the eye. B) Kinetic energy versus parallel wave-vector dispersion for the peak of the feature. A parabolic fitting gives an effective mass $m^*/m = 0.88 \pm 0.04$.

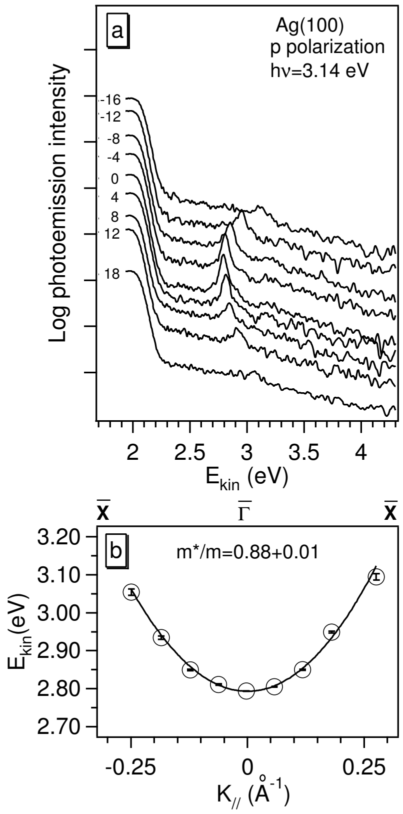

FIGURE 4.4: Multi-photon photoemission spectra from Ag(100) obtained with 150 fs, *p*-polarized laser pulses at an angle of incidence of 30° with respect to the surface normal. A) Angular dispersion of the spectral feature appearing on the high-energy electron tail along the $\bar{\Gamma}\bar{X}$ direction of the surface Brillouin zone. Each spectrum is labelled with the detection angle between the TOF axis and the surface normal. B) Kinetic energy versus parallel wave-vector dispersion for the peak of the feature. A parabolic fitting gives an effective mass $m^*/m = 0.88 \pm 0.01$.

embedded in the high-energy electron tail. The linewidth of IPS is fitted with a Lorentzian that has been convoluted with a Gaussian function to take into account the spectrometer resolution and the laser spectral width (see Appendix A). A Maxwell-Boltzmann exponential is added to the Lorentzian to fit the high-kinetic energy electron tail. The peak position of each feature is extracted from the Lorentzian parameters. Within experimental uncertainties, a different effective mass (m^*/m=0.88±0.01) is measured with respect to the direct population case (m^*/m=0.97±0.02, see Chapter 1) for both polarizations, as reported in Table 4.1.

4.5 Discussion

4.5.1 Indirect population of IPS

In Fig. 4.2B the violation of the electric dipole selection rules, normally respected in the absorption and photoemission processes from IPS on Ag(100) (see Fig. 4.2A), is reported when the sample is excited with 3.14eV-ultrashort laser pulses.

The intensity used for this experiment is of the order of 100 μJ/cm^2. In this regime, the production of high-order-harmonics at the surface can not be responsible for high-energy electron photoemission [64]. Among the possible origins of the photoemission from IPS with s polarized light, sample roughness should be ruled-out, since it must affect also direct excitations at $h\nu$=4.28 eV [33]. The evidenced violation of the selection rules implies that a dipole transition is not responsible for the population and photoemission processes, but a proper momentum conservation must be invoked.

In Chapter 3, we have shown that the *intraband* transition processes, responsible for 3.14eV-photon absorption, can be explained through a scattering-mediated mechanism. This interpretation is in the same direction as recent theoretical works [34, 35], where the scattering process responsible for the electron $k_{\parallel}$-momentum exchange is attributed to an electron-phonon collision. This interaction, during the n-photon absorption, changes only the $k_{\parallel}$ momentum and not the energy of the electrons. In this framework the violation of the dipole selection rules can be attributed to the indirect population mechanism. In Fig. 4.5 a schematic drawing of the indirect population process is reported: a) upon a

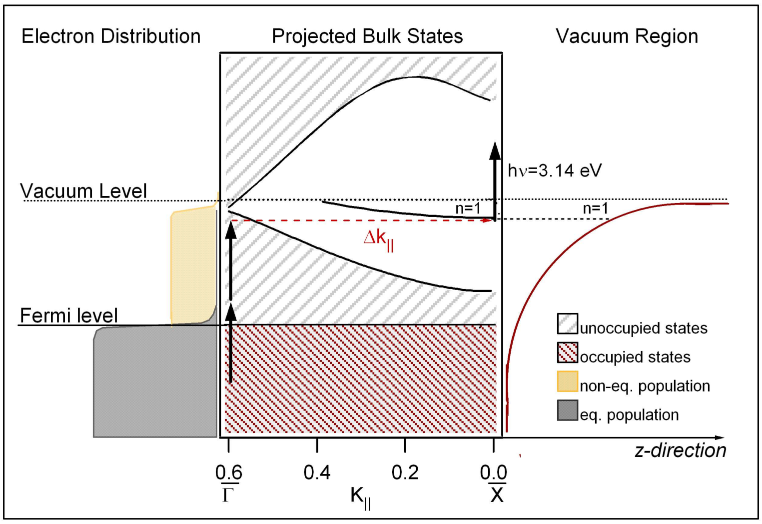

FIGURE 4.5: In the center: the projected band structure along the $\bar{\Gamma}\bar{X}$ direction of Ag(100) surface Brillouin zone is shown (taken from Ref. [9]). A possible mechanism responsible of the violation of the electric dipole selection rules is represented: a) upon the absorption of 2 photons a non-equilibrium population is created in the *s*-band at $k_{||} \neq 0$ (this process has been described in detail in Chap. 3); b) a scattering-mediated transition is responsible of the population and photoemission of IPS. On the right: the IPS potential is shown (red line) along with the binding energy of the n=1 IPS. On the left: a picture of the equilibrium and excited electron population, through two-photon absorption is reported. For graphical reasons the population excited by single-photon absorption is not reported.

2-photon absorption, the *s*-band at $k_{||} \neq 0$ is populated, b) a scattering-mediated transition is responsible for the population and photoemission of IPS.

This explanation reconciles different experimental findings, relative to the case of excitation with 3.14eV-150fs laser pulses:

- The photoemission process from IPS is a 3rd order process
- The dipole transition selection rules are no longer respected

- The photoemission from IPS strongly depends on the density of electrons excited in the conduction band of Ag(100)

4.5.2 $E_{\|}$-dependance of non-linear photoemission

The dependance on light polarization of the high kinetic energy region in the photoemission spectra reported in Fig. 4.2B, further confirms the attribution of this spectral region to a scattering-mediated 3-photon photoemission process.

In our experiment, the mean kinetic energy $\langle E_{osc} \rangle$ acquired by the electron oscillating in the field ($\langle E_{osc} \rangle = e^2E^2/4m\omega^2$, where ω, E and m are, respectively, the frequency and the amplitude of the laser field and the electron rest mass) is four orders of magnitude smaller than the photon energy ($h\nu = 3.14eV$), therefore a quantum-mechanical approach has to be considered. In this case, the electronic states of the metal are described through Volkov wavefunctions [65], i.e. free-electron wavefunctions dressed by the e.m. field. In the model proposed in Ref. [35], the scattering mechanism is attributed to an electron-photon-ion collision term, already reported in the Seely and Harris model [66]. The equation governing the absorption process is:

$$\left(\frac{\partial f(k)}{\partial t} \right)_{absorb} \propto \sum_n J_n^2 \left(\frac{e\mathbf{E} \cdot \Delta\mathbf{k}}{m\omega^2} \right) \tag{4.4}$$

where $f(k)$ is the electron distribution function, n is the number of absorbed photons, Jn is the Bessel function of order n, and $\Delta\mathbf{k}$ is the exchanged momentum during the collision (see eq. 7 in Ref. [35]). In our case only the $\mathrm{E}_{\|}$ component of the incident electric field can contribute to the electron $\Delta\mathrm{k}_{\|}$ exchange involved in the photoemission process. For this reason we expect a different intensity of the non-thermal electron population by changing the component parallel to the surface of the impinging electric field, in agreement with the results reported in Fig. 4.2B.

Using eq. 4.4, we have calculated the predicted intensity ratio due to polarization dependance, assuming that the photoemission process can be divided in two steps. The first is the absorption of one photon coupled with an electron-ion collision, and the second is the absorption of two photons during a scattering event (see Fig. 3.4 of Chap. 3). The ratio R can be expressed by:

$$R \simeq \frac{J_1^2\left(\frac{eE_P\Delta k_{\parallel}\cos(30^\circ)}{m\omega^2}\right)\cdot J_2^2\left(\frac{eE_P\Delta k_{\parallel}\cos(30^\circ)}{m\omega^2}\right)}{J_1^2\left(\frac{eE_S\Delta k_{\parallel}}{m\omega^2}\right)\cdot J_2^2\left(\frac{eE_S\Delta k_{\parallel}}{m\omega^2}\right)} \tag{4.5}$$

where E_P and E_S are, respectively, the absorbed electric field with *p*- and *s*-polarized light. In the calculation only an exchanged momentum parallel to the surface ($\Delta k_{\parallel} \simeq \pi/2a$) is considered, as previously discussed. To estimate the intensity of the high-energy photoemitted intensity, an integration of the expression giving $\partial f(k)/\partial t$ (see Eq. 4.4) during the pulse time duration, has to be performed. The ratio in Eq. 4.5 is estimated under the assumption that the time-integration gives the same contribution for *p*- and *s*-polarized light. The result of the calculation is R=0.29. This value has to be compared to the ratio I_p^3/I_s^3=0.77, which takes into account only the variation of the absorbed laser fluences during the experiments in *s* and *p* polarizations (see Section 4.4.2). The measured intensity ratio of 0.22 is close to the ratio calculated by taking into account a photoemission dependance on the direction of the incident electric-field vector (Eq. 4.5). This result is a confirmation of the hypothesis that a scattering-mediated transition is involved in the non-linear photoemission of the high-energy electron tail.

4.5.3 IPS interaction with the non-equilibrium electron distribution

In Section 4.4.3 a variation of the n=1 IPS effective mass is evidenced, when the Ag(100) crystal is excited with 3.14eV-150fs laser pulses. In this case a high-density non-equilibrium electron population ($n \simeq 10^{19}$-10^{20}electrons/cm^3) is created in the empty states of the conduction band (see Sec. 4.2). As a consequence of the results reported in Chapter 3, the equilibrium electron distribution is perturbed in a negligible way at the laser intensities (I$\simeq$ 0.1GW/cm^2) used in the experiments. For this reason the variation of the IPS effective mass can not be attributed to a perturbation of the equilibrium electron distribution, but to an interaction with the non-equilibrium population. In this frame, the IPS represent a simple model of a 2-dimensional electron gas interacting with a 3-dimensional electron distribution.

From a theoretical point of view, the problem of an interacting electron gas has been widely studied with many-body techniques. The knowledge of the electron self-energy $\Sigma^*(\mathbf{k},\omega)$, defined in Section 4.1, enables to calculate the quasi-particle energy spectrum $\epsilon_k = \hbar^2\mathbf{k}^2/2m + Re\Sigma^*(\mathbf{k},\omega)$, where m is the free-electron mass. The electron effective mass m^* is defined by $\epsilon_k = \hbar^2\mathbf{k}^2/2m^*$. Expanding ϵ_k around $k{=}k_F$ and $\omega{=}\omega_F$, we obtain the expression [67]:

$$m^*/m = \left(1 - \frac{\partial\Sigma^*(\mathbf{k},\omega)}{\partial\omega}|_{k_F,\omega_F}\right)\cdot\left(1 + \frac{m}{k}\cdot\frac{\partial\Sigma^*(\mathbf{k},\omega)}{\partial k}|_{k_F,\omega_F}\right)^{-1} \tag{4.6}$$

where k_F and $\hbar\omega_F$ are, respectively, the Fermi momentum and energy of the quantistic electron gas.

The calculation of the self-energy is usually performed in the Random Phase Approximation (RPA), i.e. the perturbative terms considered in the diagrammatic expansion of $\Sigma^*(\mathbf{k},\omega)$ are the first, the second and the ring diagrams at all orders. In this case the "screened" potential can be expressed in the form:

$$W^{RPA}(\mathbf{k},\omega) = \frac{V_k}{\varepsilon^{RPA}(\mathbf{k},\omega)} \tag{4.7}$$

where $V_k = 4\pi e^2/k^2$ is the bare Coulomb potential and ε^{RPA} is the RPA dielectric function, which takes into account the many-body interactions.

The first-order diagrammatic expansion of the self-energy can be easily calculated (for a detailed explanation see [68]), resulting in two different terms in addition to the unperturbed electron energy spectrum $\epsilon_k^{(0)}$:

$$\epsilon_k^{(1)} = \epsilon_k^{(0)} + \epsilon_{k=0} + \epsilon_k^{(exc)} \tag{4.8}$$

$\epsilon_{k=0}$ is a constant term that can be eliminated by considering a positive background (jellium) and $\epsilon_k^{(exc)}$ is the exchange energy, whose dependance on the momentum k is given by:

$$\epsilon_k^{(exc)} = -\frac{e^2k_F}{\pi}\left\{1 + \frac{k_F^2 - k^2}{2kk_F}ln\left|\frac{k_F + k}{k_F - k}\right|\right\} \tag{4.9}$$

By integrating over k, the mean exchange energy per particle (E^{exc}) is obtained. The result is a negative contribution to the total energy, because the exclusion principle tends to reduce the effect of Coulomb repulsion, by keeping apart charged particles. It is also

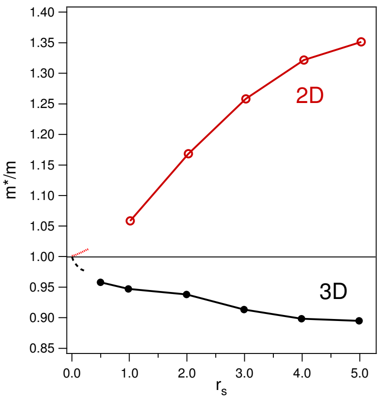

FIGURE 4.6: The effective-mass ratio m^*/m vs the Seitz radius r_s for the 3D (black filled-circles) and 2D electron gas (red empty-circles), as calculated in Ref. [67]. The black-dashed and the red-dotted lines are, respectively, the high density limits for the 3D [69, 70] and 2D [71] electron gas.

interesting that $E^{exc} \propto r_s^{-1}$, whereas the mean kinetic energy $E^{kin} \propto k_F^2/2m \propto r_s^{-2}$. For this reason, in the high density limit ($r_s \ll 1$, where r_s is the Seitz radius), the contribution of the exchange energy is expected to become negligible.

The higher perturbative terms of the electron self-energy were calculated in the high-density limit ($r_s \ll 1$) by Gell-Mann [69]. The result was that a positive term has to be added to $\epsilon_k^{(0)}$: $\epsilon_k = \epsilon_k^{(0)} + \epsilon_{k=0} + \epsilon_k^{(exc)} + \epsilon_k^{(cor)}$, where $\epsilon_k^{(cor)}$ is the correlation energy, related to the Coulomb interaction between electrons. This term gives a positive mean exchange energy per particle, proportional to: $E^{cor} \propto \ln(r_s)$. As a consequence, the contribution of the correlation energy to the total energy is also negligible in the limit $r_s \rightarrow 0$.

With the help of Eq. 4.6, it is possible to calculate the quasi-particle effective mass m^*/m related to the exchange and correlation terms. In general the result is that the exchange interaction diminishes the value of m^*/m, whereas the correlations shift it in the opposite direction.

As a confirmation of this trend, the quasi-particle effective mass has been recently calculated in the metallic region ($1 < r_s < 5$) for a 3-dimensional and a 2-dimensional electron gas [67]. In three dimensions the effective mass monotonically decreases as a function of r_s, while in two-dimensions, where correlations are stronger, the effective mass is a monotonically increasing function of r_s, as evident in Fig. 4.6.

The physics of electrons on IPS is, unfortunately, more complicated, because we have to find a model for the interaction between a two-dimensional electron gas at the metal-vacuum interface and the underlying three-dimensional electron distribution.

A simplified model as been suggested in Ref. [25], where it is assumed that the charge density and the screened potential W is constant in the x-y plane parallel to the surface and varies only in the z direction perpendicular to the surface. A schematic plot of the one-dimensional potential, called model-potential, is reported in Fig. 4.7. The model-potential takes into account the band structure of the metal, in the bulk region, and merges into the long-range image potential, in the vacuum region. In this approximation, the single-particle wavefunction has the form:

$$\Psi_{k_{\parallel}}(\mathbf{r}) = (A^{-1/2}) e^{i\mathbf{k}_{\parallel}\cdot\mathbf{r}_{\parallel}} \Phi(z) \tag{4.10}$$

where $\mathbf{r}_{\parallel}$ is the parallel coordinate, $\mathbf{k}_{\parallel}$ is the wave-vector parallel to the surface, $\Phi(z)$ describes the motion normal to the surface and A is the normalization area. By using the 2D Fourier transform of the screened interaction $W(z, \mathbf{k}_{\parallel}, \omega)$ and tuning the parameters of the model for different metals, it is possible to predict the right values for the binding energies and lifetimes of IPS in almost all cases.

So far, the problem of the interaction with a non-equilibrium population has not been studied from the theoretical point of view. Our results indicate that the coexistence of electrons at the Ag(100) surface with a 3D athermal electron gas, results in a reduction of the effective mass. The interaction responsible of the m^*-reduction, can be attributed to $k_{\parallel}$-exchanging scattering events between an electron in the IPS and the bulk electrons, as discussed in Sec. 2.7 of Chap. 2. In this frame the screened potential W does not need to contain information on the band structure of the metal and on the long-range image potential, as in the standard case, but, has to take into account the 3D and 2D energy and momentum distribution of the bulk electron gas and of electrons on IPS, respectively. Our experimental scheme is a unique tool to investigate this problem, because:

- The IPS effective mass on Ag(100) is very near to unity (see Chapter 1), allowing

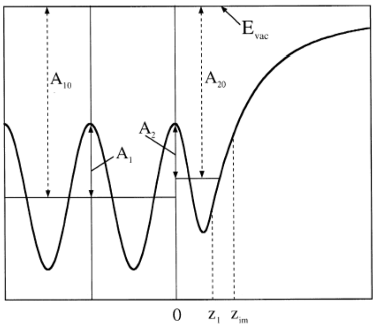

FIGURE 4.7: A schematic plot of the model potential, taken from Ref. [72], is shown. A$_1$, A$_2$, A$_{10}$, A$_{20}$, z_l and z_{im} are the parameters of the potential. Vertical solid lines represent the position of atomic layers.

to consider the electrons as a real 2D gas.

- The density of the non-equilibrium electron population is of the order of $n \simeq 10^{20}$electrons/cm^3 (see Section 4.2), so the value of the Seitz radius is about: $r_s = a_0^{-1}(3/4\pi n)^{1/3} \simeq 25$. This constitutes a low-density limit in which the exchange and correlation energies play an important role.

Our experimental result seems to indicate a reduction of the effective mass due to exchanging effect, but a further theoretical investigation is needed to properly attribute the m^*-reduction effect.

4.6 Summary

Angle-resolved non-linear photoemission spectroscopy is performed on Ag(100), with s- and p-polarized ultrashort laser pulses. A photon energy smaller than the energy difference between the IPS binding energy and the Fermi level, is used in order to investigate IPS properties in the non-equilibrium regime.

The violation of the electric dipole selection rules, normally respected in the excitation and photoemission process from IPS, is demonstrated and attributed to an indirect population mechanism.

The dependance of the high-energy electron tail on the light polarization is attributed to the scattering-mediated transitions responsible of the photoexcitation of a high-density (n $\sim$$10^{19}$-$10^{20}$ electrons/cm^3) non-equilibrium electron population in the *s*-*p* conduction band.

A value of the IPS effective mass smaller than unity (m^*/m=0.88±0.04) is measured. This result is at variance with the effective mass measured in the resonant two-photon photoemission experiment (m^*/m=0.97±0.02, see Chap. 2). This variation is attributed to a many-body interaction of electrons populating IPS with the photoinduced non-equilibrium electron population. Our results open a further theoretical investigation of the interaction between a 2-dimensional and a 3-dimensional electron system, in order to understand the role of the non-equilibrium electron distribution in the many-body interaction potential.

Chapter 5

Photo-Induced Insulator-Metal Transition in VO_2

Vanadium dioxide (VO_2) is an interesting system, exhibiting an Insulator-Metal phase transition (IMPT) at $T_c \simeq 340$ K. The IMPT results in an abrupt change of both electronic and structural properties. Recently it has been demonstrated that the IMPT of VO_2 can be induced by exciting a thin film with femtosecond laser pulses, but the physical mechanisms driving the ultrafast transition have not been clarified.

Time-resolved reflectivity in the near-IR spectral region is performed on a multi-film sample. Our results show that, after excitation with ultrashort pulses, the insulating band-gap collapses on the 150 fs timescale. In addition we demonstrate that the solid-solid transition in VO_2 can be induced with a photon energy of the incident light smaller than the electronic band-gap. This result suggests that no role is played by the density of electrons excited in the conduction band, whereas the transition dynamics is driven by the photo-induced excitation of coherent phonons.

5.1 Introduction

With the advent of femtosecond laser sources, it has been possible to investigate solid state properties in the non-equilibrium regime. In particular ultrashort coherent light pulses have been used to induce non-equilibrium heating of an organic film [73], ultrafast non thermal melting on germanium [74] and coherent lattice vibrations on bismuth [75]. More recently the possibility to optically drive structural and electronic phase transitions in solid-state systems [76, 77] or molecular crystals [78] has attracted growing interest.

In this chapter we investigate the photo-induced Insulator-Metal phase transition (IMPT) of vanadium dioxide (VO_2). VO_2 is a nonmagnetic system, with a $3d^1$ electronic configuration. The electronic properties of VO_2 are metallic-like at a temperature greater than T_c=340 K, whereas, under this temperature, an Metal-Insulator phase transition is exhibited [79]. The opening of the gap ($E_{gap} \simeq$0.7 eV) in the electronic energy bands is accompanied by a structural transition from a rutile to a monoclinic structure [80]. The origin of the band-gap has been long disputed: the issue is whether the insulating phase is due to electron correlation effects [81, 82, 83, 84, 85, 86] or whether the one-electron band picture is sufficient to describe the system and the electronic properties are typical of a band-like insulator [87, 88, 89, 90]. At the moment the problem has not been definitively solved and further experimental investigations are needed to clarify the physics of the electronic and structural properties of VO_2.

Recently it has been demonstrated that the structural and electronic IMPT can be induced if a VO_2 single crystal or thin film is irradiated by high-fluence ultrashort coherent pulses [76]. In this case the dynamics of the structural transition has been directly probed in the time-domain through ultrafast x-ray diffraction [77]. On the contrary, the simultaneous electronic phase transition has been indirectly inferred from the fact that: a) at λ=790 nm, the imaginary and real parts of the dieletric function typical of the high-T conducting phase are established after laser irradiation [76], b) a redshift in the vanadium L_3 edge is evidenced through time-resolved near-edge x-ray absorption [91]. In any case no direct measurement of the band-gap collapsing has been performed. The physical problem opened by these results concerns the fact whether the ultrafast transition is due to the photo-excitation of electrons in the conduction band or to a direct e.m. field-lattice

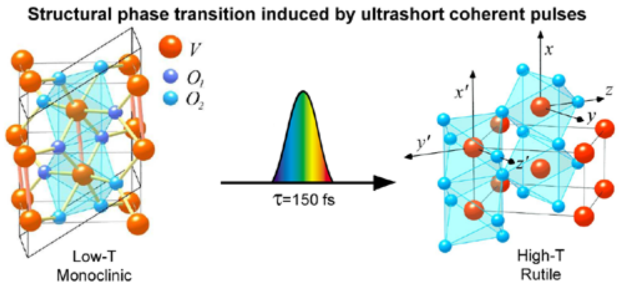

FIGURE 5.1: The Insulator-Metal phase transition in a VO_2-thin film can be induced by exciting the sample with ultrashort laser pulses. A structural phase transition from monoclinic to rutile phase is accompanied by an electronic transition from insulating to conducting state.

coupling.

We performed time-resolved reflectivity measurements on a thin film of VO_2, with a tunable femtosecond laser. By exciting the sample with 1.5eV-laser pulses (pump) and probing the transient reflectivity at a photon energy smaller than the band-gap ($h\nu$ <0.7 eV), it is possible to directly evidence the signature of the ultra-fast band-gap collapsing.

We also demonstrate that it is possible to induce the IMPT on a VO_2 thin film, with near-IR laser pulses ($0.5< h\nu <1$ eV), i.e. with a photon energy smaller than the insulator band-gap. The result that the IMPT can be induced even if the correlated d band is not highly depleted, suggests that the mechanism driving the phase transition is an e.m. field-lattice direct coupling through impulsive excitation of coherent phonons.

5.2 Temperature driven Insulator-Metal phase transition of VO_2

VO_2 differs from the many vanadium oxides (V_2O_3, V_6O_{13}), because it shows a non-magnetic ground state. The electronic configuration of vanadium dioxide is $3d^1$, so that a metallic behavior is expected. On the contrary VO_2 exhibits a first-order Metal-Insulator transition, both structural and electronic, at a temperature of about 340 K [79]. In this section we present the main features of the two phases. For a detailed discussion, see Ref. [92, 93].

5.2.1 *High-T and Low-T phases*

High-T conducting phase

The lattice structure of the High-T phase is a TiO_2-type Rutile structure (R-phase).

The schematic energy diagram for the high-T conducting phase of VO_2, is presented in Fig. 5.2 (on the left). The band structure is characterized by the fact that the oxygen $2p$ levels are well below the vanadium $3d$ states (about 2eV below the Fermi level [94]), while the latter are split, due to the octahedral crystal field, into lower t_{2g} and higher e_g levels. Furthermore the t_{2g} states, located near the Fermi level, are split into a $d_{\|}$ band, directed along the rutile c-axis and a π^* band. At $T>T_c$ the $d_{\|}$ and π^* bands overlap and cross the Fermi level, resulting in the well-known conducting properties.

Low-T insulating phase

The lattice structure of the Low-T phase is Monoclinic (M_1-phase). It is obtained from the Rutile structure by pairing and tilting of the vanadium atoms along the c-axis. This coupling results in a unit cell twice as large as that of the R-phase. In the M_1-phase, the V-V pairing causes the splitting of the $d_{\|}$ band into filled bonding and empty antibonding states ($d_{\|}^*$). The amount of the $d_{\|}$-splitting is about 2.5 eV, whereas the π^* band results upshifted of about 0.5 eV [83]. For this reason, at $T<T_c$, the Fermi level is located in the middle of the gap between the $d_{\|}$ and π^* bands and the electronic properties are insulator-like. The experimental optical gap is about 0.6 eV [94, 83].

The electronic properties of VO_2 have been long investigated both from an experimental and a theoretical point of view. Conductivity measurements were used to characterize for the first time the temperature-driven Insulator-Metal phase transition [79], while a

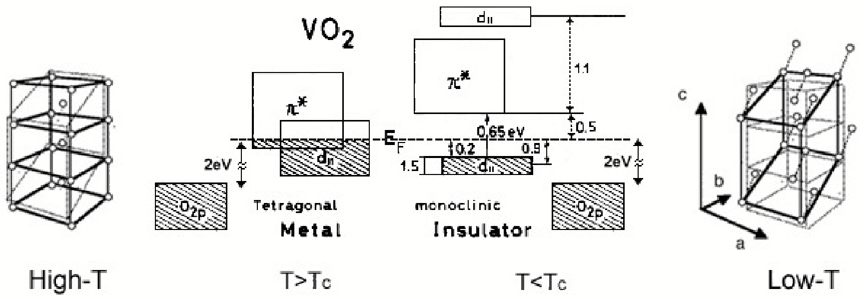

FIGURE 5.2: Schematic energy diagram of the $3d$ bands around the Fermi level for VO_2. Taken from [83]. The two crystalline structures are shown on the sides [77]. For graphical reasons only vanadium atoms are displayed. In the Monoclinic insulating phase the V-V pairing along the c-axis results in a doubling of the unit cell. In the Low-T phase a splitting of the $d_{\|}$ band is responsible of the insulating properties. A long debate has not clarified the origin of the ~0.7 eV energy gap.

following reflectivity study [94] in a wide range of wavelengths ($0.25< h\nu <5$ eV) evidenced, in the metallic phase, a Drude-like behavior of the dielectric constant at small photon energies. Later on, the VO_2 electronic structure was investigated through ultraviolet reflectance with synchrotron radiation ($2< h\nu <12$ eV), ultraviolet photoemission spectroscopy (UPS) and soft-X-rays absorption [83, 95]. The results obtained confirmed the Goodenough model [88] reported in Fig. 5.2 for the band structure of the two phases of VO_2 and evidenced the important role of electron correlation effects to justify the splitting of about 2.5 eV of the $d_{\|}$ bands. More recently temperature-dependant UPS and XPS photoemission spectroscopies were performed on a thin VO_2 film [86]. The Fermi edge in the V $3d$ spectral feature is evident at $T>T_c$. The study of the lineshape of the $3d$ band during the phase transition, evidences that, while electron-electron correlations are necessary to explain the insulating gap, electron-phonon interactions can not be neglected.

5.2.2 *Origin of the band gap at $T< T_c$*

From a theoretical point of view, different approaches have been used to study the origin of the insulating band gap in the Low-T phase, but the problem has not yet been clarified. In this section we report the main lines of the debate about this point.

The Insulator-Metal phase transition at 340 K of vanadium dioxide is characterized by a lattice distortion (from Monoclinic to Rutile phase) and a discontinuous variation of the electrical conductivity (from insulator to metal). Such an abrupt change does not allow to consider any of these variations as a consequence of the primary mechanism inducing the transition. In contrast with the evident interplay of these different aspects, the VO_2 transition has been considered, at first, a clear example of metal-insulator transition induced by lattice distortion, which causes the opening of a gap in the electronic energy levels [87, 88]. A different mechanism was proposed some years later by Zylbrsztejn and Mott [81]. They attributed the opening of the insulator gap to a strong electron-electron correlation effect in the $d_{||}$ bands. In the following years a debate was opened about the role of electrons correlations in the VO_2 band structure: the problem is whether the insulating properties are due to electron-electron correlation effects (Mott-Hubbard insulator) which stabilize the distorted monoclinic phase [82, 84, 85] or whether the one-electron approximation is still valid and the opening of the gap is simply the result of the minimization of the ground state lattice energy (Peierls insulator) [89, 90]. In this case the phase transition is driven by electron-phonon interactions. So far the issue has not yet been clarified and the problem of the subtle interplay between structure, and charge dynamics has not been solved.

From the experimental point of view, as discussed in section 5.2.1, photoemission and optical spectroscopies indicate a role both of electron-electron correlations and of electron-phonon interactions but are not able to uniquely assign the primary mechanism responsible of the insulating properties, due to the fact that, during the temperature-driven phase transition, a simultaneous variation of the different parameters is exhibited.

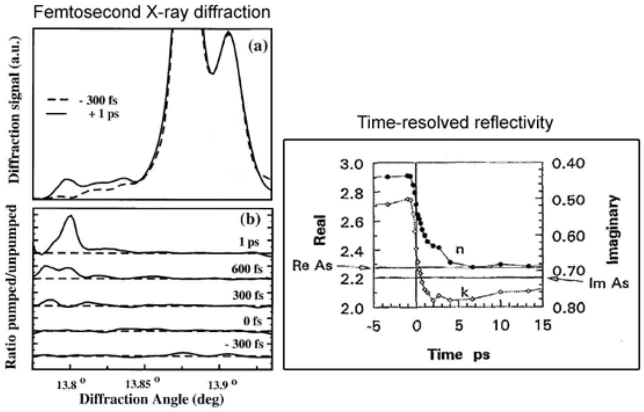

FIGURE 5.3: The Insulator-metal phase transition can be photoinduced by exciting a thin film sample of VO_2 with high-energetic ultrashort coherent laser pulses. On the left: Angle-dependent X-ray diffraction signal (a) and ratio between the X-ray reflectivity of the excited and unpumped crystal (b) at different delays between the pump and probe pulses. At an angle of about 13.8° the diffraction peak due to the photoinduced upgrowing rutile structure is evident (Taken from Ref. [77]). On the right: The photoinduced variation of the real (n) and imaginary (k) parts of the refractive index is shown. After about 15 ps the values of n and k typical of the conducting phase are established. The arrows denote the asymptotic values for n and k (Taken from Ref. [76]).

5.3 Photo-induced Metal-Insulator phase transition

A different approach to the study of the VO_2 phase transition is available, due to the advent of ultrashort coherent pulses. It has been demonstrated [76, 77] that it is possible to photoinduce the IMPT, by exciting a VO_2 sample with femtosecond pulses, at a high incident fluence (about 10 mJ/cm^2) and at a wavelength of 790 nm (1.57 eV). The investigation of the physical mechanism responsible of the ultrafast solid-solid transition constitutes an important help towards the comprehension of the origin of the insulating electronic structure of VO_2 at room temperature.

The first evidence of a photoinduced Insulator-Metal transition in VO_2 was obtained by irradiating a thin film sample in the insulating phase with 500fs-1.55eV laser pulses, at a fluence of about 5 mJ/cm^2 [76]. By probing the dynamics of the real and imaginary parts of the refraction index with 1.55eV-pulses at lower fluence, it was established that the values of the complex dielectric constant, typical of the metallic phase, are attained within 500fs from the excitation (see Fig. 5.3). The timescale of the transition dynamics is too short to be attributed to a thermal heating, induced by the laser irradiation. On the contrary the phase transition is driven by the coherent pulses through a non-equilibrium coupling mechanism.

Some years later the structural dynamics during the phase transition has been probed directly in the time-domain through femtosecond x-ray diffraction [77]. As shown in Fig. 5.3 (on the left), the photoinduced lattice distortion was detected by exciting a crystalline film of VO_2 with 20mJ/cm^2-1.55eV femtosecond laser pulses and probing it with ultrashort x-ray pulses. A few hundred of femtoseconds after the sample excitation a new peak in the diffraction signal appears, indicative of the upgrowing rutile phase. The structural transition is completed over a macroscopic volume within about 500 fs, a timescale compatible with the measured time necessary for the attainment of the metallic optical properties.

These results indicate that it is possible to photoinduce the structural transition from the M_1-phase to the R-phase of VO_2. On the same timescale, the values of refraction index at 800 nm (1.55 eV) typical of the metallic phase, are attained. However, it is important to underline that the closing of the insulating gap, during the structural transition, can not be directly inferred, as will be discussed in detail in Section 5.5.2.

More recently the photoinduced insulator-to-metal transition in VO_2 has been studied through time-resolved Near-Edge X-ray absorption [91]. Picosecond pulses of synchrotron radiation were used to probe the absorption of the vanadium L_3 edge at 516 eV, after sample excitation with 50mJ/cm^2-1.55eV laser pulses. The evidenced redshift of the L_3 edge is associated with the transient collapse of the low-temperature band gap. The time resolution of the experimental set-up is about 70 ps, a value longer than the typical time necessary for the complete phase transition (about 500fs). For this reason the measured closing of the insulating gap can not be uniquely attributed to the photoexcitation mechanism, but can simply constitute the consequence of a phase transition due to thermal heating, after the sample irradiation.

In general all the experimental measurements are performed by exciting the insulating sample with a pump pulse at a wavelength of 800 nm (1.55 eV). As evident from Fig. 5.2, this photon energy is sufficient to photoexcite electrons from the valence $d_{\|}$ filled band to the unfilled conduction band. At the fluences necessary to induce the IMPT (I>10mJ/cm^2), the density of absorbed photons ranges from 20% to 100% of the valence-band electrons [96], resulting in a heavy depletion of the $d_{\|}$ band, after laser excitation. For this reason the simultaneous excitation of two possible pathways does not allow to discriminate which is the primary mechanisms inducing the phase transition:

- If electron-electron correlations in the $d_{\|}$ band are the primary origin of the insulator band-gap, the photoinduced hole-doping can cause the collapse of the insulating electronic band structure into the metallic one.
- If VO_2 can be considered a band-like insulator, a direct excitation of coherent phonons [97] can take place and determine the femtosecond switching from the M_1-to the R-phase [77, 91].

In addition to the problem concerning the mechanism responsible of the photoinduced phase transition, the similar measured timescales for the structural and electronic bands modifications, do not allow to clarify which is the primary mechanism driving the phase transition. In a recent work [96], the transient reflectivity during the photoinduced IMPT has been measured with shorter laser pulses. The result is that, when the time-width of the pump pulse is about 15 fs, the time scale of the transition is about 80 fs. This bottle-neck corresponds to half period of the phonon connecting the two crystallographic phases and seems to indicate that an important role in the phase transition dynamics is played by the impulsive coherent excitation of a zone-edge phonon. In any case the question whether it is the electronic band collapse to drive the structural rearrangement or viceversa, is still opened.

From the technological point of view, due to the fact that the photoinduced solid-solid transition is completed within a few hundred of femtoseconds and is reversible, it may be useful for the development of ultrafast devices. In particular, the femtosecond variation of the optical properties can be applied to develop optical switches, whereas the prompt change of the lattice structure is useful for Bragg switching devices.

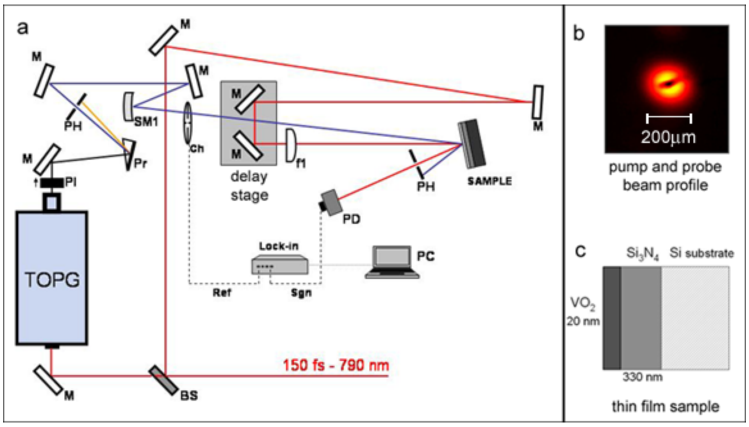

FIGURE 5.4: a) A schematic picture of the experimental set-up is shown. The light source is a TOPG, whose output spans an energy range of 2470-1200 nm (0.5-1 eV). The intensity of the reflection of the probe on the sample, is measured with a photodiode and a lock-in amplifier. The reference signal for the lock-in is the pump-chopping frequency. b) The pump and probe beam-profiles are shown. The typical FWHM of the gaussian profiles are: 200μm for the pump (in yellow-red-black intensity scale) and 50μm for the probe (the black spot in the center). c) The sample is 20nm-thin film of VO_2 on a Si(111) wafer, with a 330nm-Si_3N_4 buffer layer. The thickness of the VO_2 and Si_3N_4 films is estimated through reflectivity measurements in the 300-800 nm range.

5.4 Experimental set-up

In this section we describe the experimental set-up developed for time-resolved near-IR reflectivity measurements, shown in Fig. 5.4a.

The light source is constituted by a TOPG pumped by an amplified Ti:Sapphire laser system. The output of the TOPG is a train of 150 fs-pulses at a repetition rate of 1kHz and with an average power of about 50 mW. The *signal* of the TOPG is constituted by radiation with tunable wavelength in the range of 1600-1200 nm (0.78-1 eV), whereas the wavelength of the *idler* (for a detailed discussion refer to Par. 2.4 of Chap. 2) spans the range 2470-1600 nm (0.50-0.78 eV). The output of the TOPG is directed to the sample through a polarizer (**Pl**), to alternatively stop the cross-polarized *signal* and *idler*. A prism (**Pr**) with a Al-coated side and a pin-hole (**PH**) are used to filter the residual wavelengths in the output light (e.g. the 790nm-pump or the sum-frequency of pump+signal).

In the configuration for the near-IR pumping (the one shown in Fig. 5.4a), the output of the TOPG is focused on the sample through a spherical gold mirror (**SM1**) and is chopped at about 300 Hz before exciting the sample. A small fraction of the 790nm-pump, taken from a beam splitter (**BS**) is used as probe. A delay time τ is introduced between the *pump* and *probe* pulses through a Delay Stage, constituted by two metallic mirrors (**M**) mounted on a linear translator with a minimum step of 1μm (3 fs). The probe is then focused on the sample through a lens with focal length **f1**=300 mm. The pump and probe pulses are time and spatially overlapped on the sample and the intensity of the reflection of the probe on the sample, is measured with a photodiode and a lock-in amplifier. By using as a reference the 300Hz-trigger of the chopper (**Ch**), it is possible to directly measure the variation of reflectivity at the probe wavelength, induced by the pump exciting the sample. The reflectivity variation ($\Delta R/R$) at 300 Hz is acquired on a PC.

In the configuration for the near-IR probing (see Sec. 5.5.3), a larger fraction of the 790nm-pump is taken from the beam splitter (**BS**) and used to excite the sample. The lens **f1** is replaced by a lens with a focal length f2>f1, in order to obtain a larger beam size on the sample. The chopper (**Ch**) is moved on the 790nm-pump beam and the intensity of the reflection of the TOPG output on the sample, is measured with a photodiode and a lock-in amplifier.

In Fig. 5.4b the pump and probe beam-profiles are shown. The image is obtained by subtracting the probe from the pump profiles, separately acquired with a 14-bit CCD. The focal lengths of the spherical mirror (**SM1**) and of the dielectric lenses (**f1** and **f2**) are chosen in order to have the size of the probe gaussian-beam smaller than the pump. This configuration is studied in order to assure that the spatial region probed by the reflectivity measurement has been uniformly excited by the pump pulse and in order to avoid any problems due to slight misalignment of the two beams during the experiment. The typical Full-Width-Half-Maximum (FWHM) for the pump and probe beams is, respectively, 200 and 50 μm.

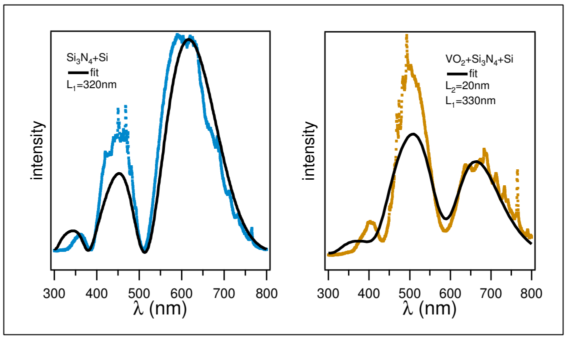

FIGURE 5.5: Reflectivity as a function of the wavelength is measured for the Si_3N_4+Si sample (left, blue dots) and for the VO_2+Si_3N_4+Si (right, yellow dots) sample. The black lines in the two graphs are the best-matching fits to the reflectivity intensities, taking into account the thickness of the different films. The values of the thicknesses estimated are: 320±10 nm for the Si_3N_4 buffer layer only, and (20±5)+(330±10) nm for the VO_2+Si_3N_4 film.

The time and spatial overlapping of the pump and probe pulses is checked by replacing the VO_2 sample with a non-linear BBO crystal and optimizing the sum-frequency generation. The pulse time-width is measured by background-free, autocorrelation of the sum-frequency generation signal. The typical time-width is of the order of 150 fs.

The sample used for the experiments is a thin film of VO_2 on a Si(111) wafer, with a Si_3N_4 buffer layer (see Fig. 5.4c). In order to evaluate the thickness of the VO_2 and Si_3N_4 films, we have performed reflectivity measurements of the VO_2+Si_3N_4+Si multi-layer and of a sample constituted by the Si_3N_4 buffer layer on the Si substrate. The light source is a CW lamp, with a wide wavelength-range emission spectrum (300-800 nm). In Fig. 5.5 the results for the Si_3N_4+Si and for the VO_2+Si_3N_4+Si multi-films are reported. The reflectivity curves obtained are characterized by an oscillatory behavior as a function of the probing wavelength. These features are due to interference effects related to the thin-film structure of the samples. To extract the VO_2- and Si_3N_4-film thicknesses (Δx and Δy, respectively), we have calculated the reflectivity of a three-layer structure as a function of Δx and Δy. The values of the real and imaginary parts of the refraction index (n and k)

in the 300-800nm wavelength-range, are taken from [98] for Si and Si_3N_4 and from [94] for VO_2. The best matching between the experimental and the theoretical curves are: Δy=320±10 nm for the Si_3N_4 buffer layer only and Δx=(20±5) nm, Δy=(330±10) nm for the multi-film sample. These last values will be taken as the film-thicknesses in the following.

5.5 Results and Discussion

5.5.1 Time-resolved near-IR reflectivity: a key to investigate the phase transition dynamics

We study the photoinduced Insulator-Metal phase transition in VO_2 with a laser source tunable in the near-IR spectral region (0.5-1 eV). Two different aspects of the ultrafast solid-solid phase transition are investigated:

- We measure the time evolution of the optical properties in the under-gap energy region ($E_{gap} \simeq$0.7 eV) and evidence the dynamics of the supposed band-gap collapse during the photoinduced IMPT of VO_2.
- We use high-fluence laser pulses, with a photon energy smaller than E_{gap}, to induce the IMPT. This experimental configuration overcomes the problem of a simultaneous excitation of the lattice structure and of the electronic distribution, because, in this regime, the photoinduced hole-doping in the $d_{\|}$ band is highly reduced. This approach constitutes an improvement towards the understanding of the mechanism responsible of the VO_2 insulating ground state at room temperature.

5.5.2 Near-IR reflectivity: band-gap signature

In Fig. 5.6 (left) the real and imaginary parts of the VO_2 dielectric function [94] are shown for the metallic and insulating phase. The behavior of the imaginary parts for the two phases is similar in the region between 1.2 and 5 eV, whereas they diverge at photon energies smaller than 1 eV. To understand the physical meaning of the energy-dependance

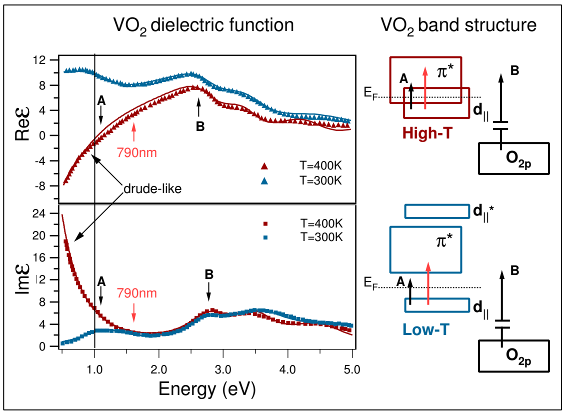

FIGURE 5.6: On the left: the real (on the top) and imaginary (on the bottom) parts of dielectric function of metallic (red dots) and insulating (blue dots) vanadium dioxide are shown. The data are taken from Ref. [94]. The solid lines are the calculated dielectric functions with a simple Drude+Oscillator model. At a photon energy smaller than about 1 eV (A-arrow) the difference between the dielectric functions of the metal and insulating phases is evident. In particular the High-T dielectric function shows a Drude-like behavior. At about 3.8 eV the kink due to the $O_{2p} \rightarrow V_{3d_\pi}$ interband transition is marked by a B-arrow. Previous measurements of the photoinduced variation of the reflectivity were performed at 790 nm (red arrow), where the optical properties are dominated by $3d_{||} \rightarrow 3\pi^*$ transitions. On the right: a schematic picture of the VO$_2$ energy bands is shown.

---

of the VO$_2$ optical properties, we have calculated the complex dielectric functions $\varepsilon(E)$ for the two phases with a simple model. For the metallic phase we assume a Drude-like behavior for photon energies smaller than 1.2 eV and a simple-oscillator behavior for photon energies greater than 1.2 eV:

$$\varepsilon(E) = \varepsilon_\infty - \frac{E_{p1}^2}{E^2 + iE/\tau_1} - \sum_{j=2}^{4} \frac{E_{pj}^2}{E^2 - E_{0j}^2 + iE/\tau_j} \tag{5.1}$$

where the first term ε_∞ represents a constant contribution to the real part of the dielectric functions from high-frequency electronic transitions; the second term is a Drude-like con-

TABLE 5.1: Values of the parameters used to fit the measured values of the complex dielectric function of VO$_2$ (Fig. 5.6) with the models reported in Eq. 5.1 and 5.2. The values of E_{pj} and E_{0j} are expressed in eV, whereas τ_j is expressed in eV^{-1}. The bold values refer to the Drude-like dielectric function of the VO$_2$ conducting phase.

		$h\nu < 1.2 eV$			$h\nu > 1.2 eV$								
	ε_∞	E_{p1}	E_{01}	τ_1	E_{p2}	E_{02}	τ_2	E_{p3}	E_{03}	τ_3	E_{p4}	E_{04}	τ_4
High-T	4.4	**3.6**	**0**	**1.3**	3.2	2.8	1.2	3.6	3.5	1.2	3.8	4.5	1
Low-T	4.5	1.65	1.25	1.1	2.8	2.8	1.2	4.25	3.6	0.9	5.6	4.9	0.5

tribution due to free-carriers, where E_p is the plasma frequency related to the density of carriers and τ represents a collision time; the third is an harmonic oscillator term, which takes into account interband transitions, where E_{pj} and τ_j are fitting parameters and E_{0j} is the resonance-energy. The values for the parameters obtained by the best matching between the experimental (red dots) and calculated (solid red lines) curves, are reported in Table 5.1.

For the insulating phase we assume only a simple-oscillator behavior:

$$\varepsilon(E) = \varepsilon_\infty - \sum_{j=1}^{4} \frac{E_{pj}^2}{E^2 - E_{0j}^2 + iE/\tau_j} \tag{5.2}$$

where the first term ε_∞, E_{pj}, E_{0j} and τ_j are, similar to the previous case, fitting parameters. The values for the parameters obtained by the best matching between the experimental (blue dots) and calculated (solid blue lines) curves, are reported in Table 5.1.

By comparing the results obtained, with the VO$_2$ band structure (Fig. 5.6, on the right), it is evident that the kink at 2.8 eV in the dielectric function curve, is related to the $O_{2p} \rightarrow V_{3d_\pi}$ interband transition, whereas the oscillator at 1.25 eV, related to the band-gap in the insulating phase, is replaced by a Drude-like term in the metallic phase.

In this framework, the variation of the optical properties between the two phases in the near-IR region ($h\nu$ <1 eV) is a fingerprint of the band gap collapse. On the

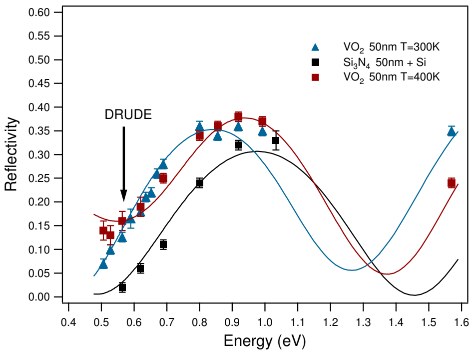

FIGURE 5.7: Reflectivity as a function of the photon energy is measured for the Si_3N_4+Si sample (black squares) and for the VO_2+Si_3N_4+Si in the metallic (red dots) and insulating (blue triangles) phases. The calculated reflectivities (solid lines) for the multi-film structure are shown. At energies smaller than 0.6 eV, the influence of the Drude-like dielectric function is evident for the High-T phase.

---

contrary, so far, only time-resolved measurements at 1.55eV-790nm have been performed. At this wavelength the optical properties of VO_2 are mainly determined by direct electronic transitions between the $d_{\|}$ and the π^* bands (see Fig. 5.6). For this reason the result that, after irradiating the insulating VO_2 with ultrashort pulses, the 790nm-reflectivity of the High-T phase is attained, can not be considered as a direct measurement of the collapsing band-gap, but only indicates that, on a femtosecond timescale, a shifting of the π^* band similar to the High-T phase is induced.

From the expression of the dielectric function, the real (n) and imaginary (k) refraction indexes can be obtained from the relation:

$$Re(\varepsilon) - iIm(\varepsilon) = (n - ik)^2 \tag{5.3}$$

In Fig. 5.7, the reflectivity of the buffer-layer (Si_3N_4+Si, black squares) and of the three-layer sample (VO_2+Si_3N_4+Si) in the metallic and insulating phases (red and blue dots, respectively) is measured as a function of the photon energy in the near-IR region. The Insulator-Metal transition is obtained by heating the sample to a temperature of about 400K. The reflectivity measurements have been performed with a GaAs photodiode, with a linear response in the region between 0.7-1 eV. At photon energies smaller than 0.7 eV, the photodiode has been used in the two-photon absorption regime. Calibration of the GaAs non-linear response has been made through the comparison with a bolometer.

The VO_2 and Si_3N_4 thicknesses, estimated in Sec. 5.4 (20 and 330 nm, respectively), and the complex refraction index, calculated through equations 5.1, 5.2, 5.3, have been used to calculate the reflectivity of the three-layer structure. The estimated reflectivity (solid lines in Fig. 5.7) is in agreement with the measured values in the 1-0.5 eV energy range. At photon energy smaller than 0.6 eV the influence of the Drude-like term of the dielectric function is evident. The consequence is a sharp increase of the reflectivity in the metallic phase, associated with the closing of the band-gap.

5.5.3 Femtosecond band-gap closing

In order to directly measure the supposed closing of the insulating band-gap during the photoinduced IMPT, we have performed time-resolved reflectivity experiments on the VO_2 multi-film sample. The IMPT is induced, as reported in literature [76, 77, 91, 96], by exciting the sample with 1.57 eV-150 fs pump pulses, at a fluence of about 80 mJ/cm^2, larger than the 10 mJ/cm^2-threshold necessary for the transition. The transient reflectivity is probed with 0.54 eV-150 fs probe pulses, at a fluence smaller than 100 μJ/cm^2, to not perturb the photoexcited system. As discussed in Section 5.5.2, the probe energy of 0.54 eV, is smaller than the band-gap ($E_{gap} \simeq$ 0.7 eV). The results are reported in Fig. 5.8.

A sharp increase of the reflectivity is measured after the pump excitation, whereas a plateaux-like behavior of the optical properties is evident at delays larger than 150 fs between the pump and the probe pulses. The measured value of reflectivity variation (ΔR/R$\simeq$+100%) is compatible with the expected variation when the phase transition is induced by changing the sample temperature, as discussed in Section 5.5.2. In fact, as reported in Fig 5.7, the reflectivity of the multi-film sample, at 0.54 eV, is about R$\simeq$0.09, in the insulating phase, and 0.18 in the metallic phase, where the Drude-like behavior of the dielectric function is dominant.

It is important to stress that previous transient reflectivity measurements were per-

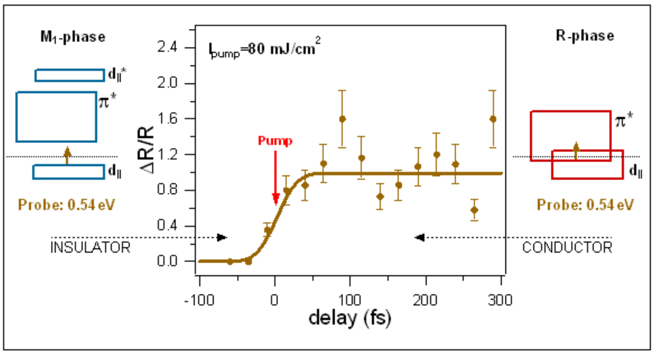

FIGURE 5.8: Time-resolved reflectivity is performed on the VO$_2$ multi-film sample. In the graph the transient reflectivity is plotted as a function of the delay between the pump and the probe pulses. In order to photoinduce the Insulator-Metal phase transition, the photon-energy of the pump pulse is 1.57 eV (790 nm), with a fluence of about 80 mJ/cm^2,. The induced reflectivity variation is measured in the under-gap energy region, with a probe photon energy of 0.54 eV. The doubling of the 0.54 eV-reflectivity is the signature that the band-gap collapse is completed within 150 fs from the excitation.

formed at a probing wavelength of 790 nm, where the optical properties are dominated by $3d_{\|} \rightarrow 3\pi^*$ transitions. As a consequence the reflectivity of the sample was measured to decrease of about 20%, after laser irradiation [77, 91, 96]. The negative reflectivity variation is reported in the next chapter, where the IMPT is probed at a wavelength of 790 nm (see Fig. 5.9-5.11).

Our results demonstrate that, within 150 fs from laser irradiation, the insulating band-gap collapses and the metallic optical properties are attained. This fact constitutes the first direct evidence that the photoinduced structural phase transition in VO$_2$ is accompanied by the electronic phase transition and by the closure of the ~0.7 eV band-gap. The 150 fs timescale of the electronic transition, constitutes the evidence that the thermal heating of the system, due to laser irradiation, is not involved in the process, but the variation of the electronic properties is directly driven by the ultrashort laser pulse.

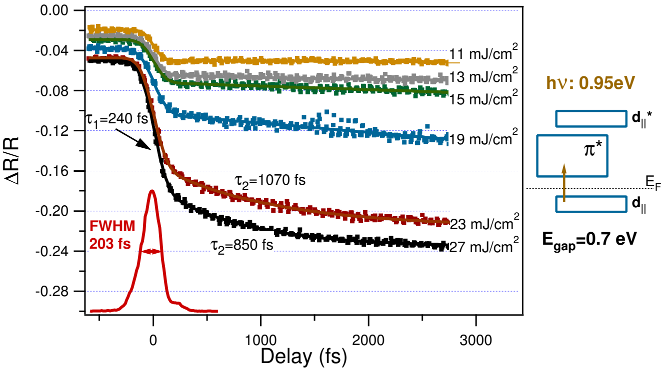

FIGURE 5.9: Time-resolved reflectivity is performed on the VO$_2$ sample. The photon energy of the pump pulse is 0.95 eV, a value greater than the band-gap (E_{gap} $\simeq$0.7 eV). The fluence of the pump beam spans the range between 11 and 27 mJ/cm^2. The probe is the 790nm-Ti:Sapphire fundamental. Two different dynamics are evident: within the laser pulse duration a sharp variation, up to the 20%, is measured; a slower decrease of about 4% follows the first dynamics. This effect is more evident at high pumping fluences. The FWHM of the autocorrelation of laser pulse on the BBO crystal is about 200 fs (solid red line).

5.5.4 Photoinduction of the Insulator-Metal phase transition at different photon energies

In this section we describe time-resolved reflectivity measurements performed on a VO$_2$ thin film by inducing the IMPT in the under-gap region ($h\nu < E_{gap}$) and probing the reflectivity variation at 790 nm. The aim of this new excitation-scheme is to highly reduce the density of hole-doping in the $d_{||}$ band, due to pump excitation, and evidence the mechanism responsible of the ultra-fast solid-solid transition. The experimental set-up is changed, with respect to the previous experiment, as described in Section 5.4.

In Fig. 5.9 the transient reflectivity measurements obtained by exciting the sample at a photon energy of 0.95 eV ($h\nu > E_{gap}$), with different laser intensities, are shown. At an incident fluence of 27 mJ/cm^2 the reflectivity variation $\Delta R/R$, measured 2 ps after the sample excitation, is about -24%. This decrease of the sample reflectivity is compatible with the optical properties of the metallic phase, measured when the phase transition is induced by changing the sample temperature. In fact, as reported in Fig. 5.7, the reflectivity of the thin film sample at 790 nm in the insulating and metallic phase is, respectively, 0.35 and 0.24, resulting in $\Delta R/R$=-30%. The slight discrepancy with the measured value can be attributed to the fact that the intensity profile of the pump pulse results in a non-uniform excitation of the sample and, as a consequence, the reflectivity measured by the probe pulse has to be considered as a spatial average over the probe area. After the pump excitation a two-step dynamics is evident: a) within the laser pulse duration a sharp decrease of the reflectivity, up to -20%, is measured; b) a slower variation of about -4% on the picosecond scale is observed. The first femtosecond dynamics can be considered as the signature of the photoinduced-phase transition, whereas the second dynamics seems to be related to the structural distortions of the regions of the film near the volume promptly transformed by the pump pulse. This effect has been already reported [91] on a film with a thickness (about 200 nm) larger than the penetration depth (160 nm). When the incident fluence is reduced, the measured reflectivity variation $\Delta R/R$ is smaller, suggesting that the phase transition has not been uniformly induced over the probe area.

In Fig. 5.10 a long-range and a short-range time-resolved reflectivity measurement, in the same experimental configuration than before, is reported. In the graphic on the top, the fast femtosecond dynamics is evidenced. The sharp reflectivity variation indicates that the timescale of the photoinduced transformation, is shorter than the laser timewidth ($\tau = FWHM/\sqrt{2} \simeq$150 fs). This result has to be interpreted as the experimental evidence that the induced phase transition is not driven by a thermal effect. In fact any interpretation in terms of local heating of the lattice, due to the laser excitation, has to be ruled out, because the typical timescale for electron-phonon thermalization is of the order of picoseconds. On the bottom of Fig. 5.10, the picosecond evolution of the VO_2 reflectivity is reported. After about 10 ps, a constant value of the reflectivity is measured, indicating that the photoinduced metallic state can be considered as a metastable state. A slow return to the insulating phase is obtained through heat diffusion on the nanosecond timescale [91]. It is important to underline that at negative delay values, $\Delta R/R$ is different from zero (see Fig. 5.10). This can be a signature of a longer structural relaxation-time (τ_3) that can be

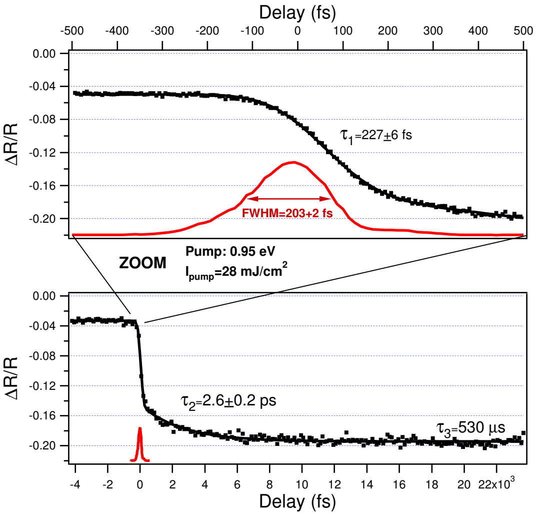

FIGURE 5.10: Time-resolved reflectivity is performed on the VO$_2$ multi-film sample, with a photon energy of the pump pulse of 0.95 eV. The two-step dynamics reported in Fig. 5.9 is evident. Within 10 ps from the photoexcitation, a constant reflectivity is measured (on the bottom), indicative of a metallic metastable phase. The insulating phase is slowly recovered via heat diffusion. On the top of the figure a short-range measurement is shown. Within the laser pulse duration (about 150 fs) the prompt variation of the reflectivity is completed. The timescale necessary for the electronic and structural phase transition is incompatible with a thermal effect. The FWHM of the autocorrelation of laser pulse on the BBO crystal is about 200 fs (solid red line).

---

evaluated by fitting the experimental curve with a decreasing exponential function, which assumes the values -0.2 at a delay of 10 ps and -0.04 at 1 ms, which is the temporal distance between two pulses. The result is $\tau_3 \sim 500\mu$s, a value compatible with a macroscopic structural rearrangement.

In Fig. 5.11 the time-resolved reflectivity variation induced on the VO$_2$ sample by excitations at different wavelengths is shown. In particular the IMPT can be induced with photon energies in the range of 0.6-0.5 eV, values smaller than the insulating band-gap (E_{gap} $\simeq$0.7 eV).

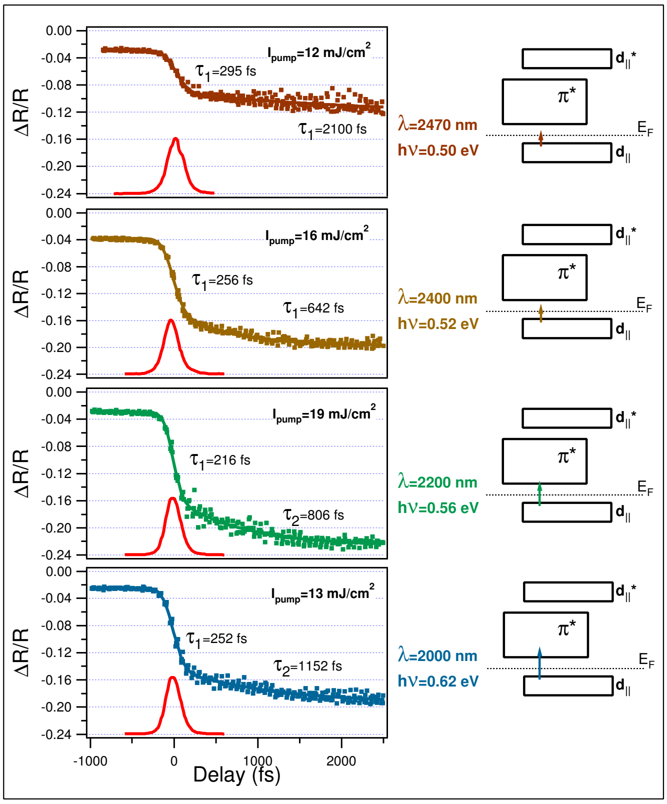

FIGURE 5.11: Time-resolved reflectivity on the VO_2 is performed at different photon energies of the pump pulse. It is evident that the phase transition is induced, even when $h\nu$ is considerably smaller than the band-gap. The incident fluence necessary to photoinduce the IMPT is similar for every wavelength used. This results indicate that the induction of the phase transition is not correlated to the density of electrons excited in the conduction band, suggesting a direct e.m. field-lattice coupling mechanism. The FWHM of the autocorrelation of laser pulse on the BBO crystal is about 200 fs (solid red line).

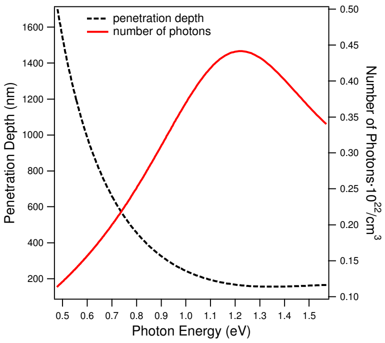

FIGURE 5.12: The calculated penetration depth of VO_2 as a function of the photon energy of the pump pulse is reported (black dashed line). In addition the number of absorbed photons has been calculated for an incident laser fluence of 15 mJ/cm^2 (red solid line). The VO_2 density is about $3{\cdot}10^{22}$cm^{-3}.

To evaluate the hole doping induced in the $d_{||}$ band at different photon energies, we have calculated the density of photons absorbed by the VO_2 thin film. By neglecting thin-film effects, the penetration depth L is given by:

$$L = \frac{\lambda}{4\pi k} \tag{5.4}$$

where k is the imaginary part of the refraction index and λ the light wavelength. The values of k at different wavelengths are taken form the data reported in Fig. 5.6. In Fig. 5.12 the obtained penetration depth as a function of the photon energy is reported (black dashed line). In addition the number of absorbed photons has been calculated for an incident laser fluence of 15 mJ/cm$_2$ (red solid line). The result is that the density of electrons excited from the $d_{||}$ band is decreased by a factor three, ranging from 1 to 0.5eV-photon energy. This is the consequence of the decreasing value of k in the under-gap energy region of the insulating VO_2 (see Fig. 5.6). For this reason, if the phase transition is related to the hole doping of the $d_{||}$ band, we expect an increase of the fluence necessary to induce the IMPT at a photon energy of 0.5-0.6 eV, with respect to the case of 1eV-excitation. On the contrary, as evident from Fig. 5.12 and 5.9, the incident fluence needed to induce the IMPT decreases from 20-25 mJ/cm^2 at a photon energy of 0.95 eV, to 15-20 mJ/cm^2 at

0.5-0.6 eV photon energy.

We have demonstrated that the Insulator-Metal phase transition of vanadium dioxide can be induced by exciting a thin -film sample with high-fluence ultrashort coherent pulses, with a photon energy smaller than the insulating band-gap. This result indicates that the density of the hole photo-injected in the $d_{\|}$ band does not play any role in the process. As a consequence, the photoinduced removal of electron correlations in the valence band has to be ruled out as a possible mechanism responsible of the ultrafast phase transition. Our results suggest, on the contrary, that a direct coupling between the e.m. field and the lattice is involved.

Recently it has been demonstrated [96] that, by exciting a VO$_2$ thin film with low-fluence (few order of magnitude lower than needed to induce the IMPT) femtosecond laser pulses, it is possible to coherently excite two Raman-active phonons modes, with A$_g$ symmetry. These phonon modes disappear in the High-T phase and play an important role in the connection of Rutile and Monoclinic lattice structures. In this framework, a possible explanation of the photoinduced IMPT can be constituted by the coherent excitation of these phonon modes, through high-fluence ultrashort laser pulses: on the femtosecond timescale, the lattice is coherently switched to the High-T structure an the metal phase is established.

This far-from-equilibrium process, has important implications on the understanding of the equilibrium electronic properties of insulating VO$_2$. In fact the result that the photoinduced electronic phase transition is a consequence of the structural rearrangement due to the lattice-e.m. field coupling, suggests that the band-like character can be predominant in the determination of the VO$_2$ electronic properties.

5.6 Summary

Time-resolved reflectivity spectroscopy in the near-IR ($1200< \lambda <2400$ nm) spectral region is performed on a thin film of VO$_2$, in order to study the photoinduced Insulator-Metal phase transition.

After the excitation of the sample with high-fluence 1.57eV-femtosecond pulses, an increasing of 100% of the reflectivity at 0.54 eV is measured. This variation is the fingerprint of the insulating band gap collapse on the ∼150 fs timescale. This result constitutes the first direct evidence that an electronic phase transition coexists with the structural phase transition, induced by laser irradiation.

The Insulator-Metal phase transition (IMPT) is also induced by exciting the film with femtosecond pulses in the under-gap region (E<0.7 eV). We demonstrate that the fluence necessary to induce the IMPT does not dependent on the photon energy of the incident light. This result suggests that the mechanism driving the non-thermal solid-solid transition is independent on the density of holes photoinjected in the $d_{\|}$ band. A possible explanation attributes the ultrafast phase transition to the photo-induced excitation of coherent phonons. Our results constitute an important step towards the understanding of the physical mechanism responsible of the insulating properties of VO_2 at room temperature and towards the optical control of solid-solid phase transitions.

Chapter 6

Conclusions

6.1 Summary

In this thesis two relevant topics in ultrafast solid-state physics have been investigated. In particular, the interaction between Image Potential States on Ag(100) and the non-equilibrium population excited in the empty bands and the Insulator-to-Metal phase transition in VO_2, induced by irradiating a thin-film with ultrashort coherent pulses, have been studied. The common feature of the two problems is the attempt to achieve optical control of non-equilibrium solid state properties.

Image Potential States on Ag(100)

Time-resolved and angle-resolved photoemission spectroscopy is performed on Ag(100), in order to study the Image Potential States properties in the non-equilibrium regime. We have demonstrated that it is possible to create, by selecting the appropriate excitation channel, a transient two-dimensional electron gas (IPS) at the metal surface, coexisting with a transient three-dimensional electron gas in the underlying bulk states (the photoinduced non-equilibrium electron population). As a consequence the IPS properties change, due to many-body electron interactions.

This simple system constitutes a promising model to study, in the time-domain, the dynamics of electron screening at a metal-vacuum interface.

Insulator-Metal phase transition in VO_2

The Insulator-to-Metal phase transition in vanadium dioxide is investigated via time-resolved reflectivity spectroscopy in the near-IR spectral region. We have demonstrated the collapse of the insulating band-gap, on the femtosecond timescale, by irradiating a VO_2 thin film with ultrashort pulses. In addition, we have discriminated between possible physical mechanisms responsible for the ultrafast structural and electronic phase transition by selective tuning of the exciting photon energy. In particular, we have demonstrated that the impulsive excitation of coherent phonons plays a dominant role.

The interest in this system is both technological and scientific. The optical control of the VO_2 lattice and electronic structure has far reaching implications for the development of ultra-fast solid-state devices; furthermore it is of great help in understanding the mechanisms driving the system from the ground state to the photoinduced metastable state.

In this work we have demonstrated the possibility of selecting a particular excitation channel by tuning the photon energy of the incident light. This is a step towards the coherent control of electronic interactions responsible for the macroscopic properties of interesting materials, such as strongly-correlated systems. The coherence between the exciting e.m. field and the electron population can be preserved if the timescale necessary to remove o induce electron-electron many-body interactions is smaller than the timescale necessary to recover the equilibrium properties, via electron-electron scattering. In this framework, it is possible to study the effect of the prompt removal of electron-electron screening in correlated systems, through excitation with tunable femtosecond light pulses. This is in the direction of the achievement of coherent manipulation of the macroscopic properties of condensed-matter systems.

Appendix A

Influence of the spectrometer resolution on intrinsic linewidth measurements at $\mathbf{k}_{\|} \neq \mathbf{0}$

The knowledge of the intrinsic linewidth of image potential states as a function of parallel momentum helps in discriminating which mechanism contributes to the IPS decay, as discussed in Chapter 1. To achieve a better estimate of the intrinsic linewidth we propose a new fitting procedure that accounts for the influence of the angular acceptance of the detector. The predictions of this improved fitting procedure are tested comparing measurements taken with two TOF, having different angular resolution.

A.1 Problems of $\mathbf{k}_{\|}$-resolution: a new fitting procedure

The experimental UHV chamber is equipped with two Time of Flight spectrometers with different energetic resolution (see Section 1.5 of chapter 1):

- *Low Resolution* TOF:
  - geometrical acceptance angle = ±2.6°
  - time-to-amplitude converter resolution = 0.5 ns
  - overall energy resolution
    (detector resolution + laser linewidth) = 45 meV @ 2 eV
- *High Resolution* TOF:
  - geometrical acceptance angle = ±0.83°
  - time-to-amplitude converter resolution = 0.25 ns
  - overall energy resolution
    (detector resolution + laser linewidth) = 35 meV @ 2 eV

In Fig. A.1 the 2PPE spectra, acquired on a Ag(100) single crystal, with a photon energy of 4.32 eV and at $k_{\|}$=0 with the high resolution TOF (a) and with the low resolution TOF (b), respectively, are shown.

The effective mass associated with the n=1 IPS electrons has been measured along the direction of the surface Brillouin zone (SBZ), resulting in a value of 0.97±0.02 in free-electron mass units (see Chapter 1). The binding energy [1] of n=1 IPS feature is 0.4±0.1eV in agreement with the values reported in the literature [11]. The two sets of photoemission measurements are collected by changing the angle between the normal to the sample and the TOF axis, along the $\overline{\Gamma X}$ symmetry direction of the Ag(100) SBZ in order to trace the $k_{\|}$-dispersion of the IPS states [18]. In order to estimate the intrinsic linewidth, a study of the lineshape of these states is performed. In particular, the n=1 IPS feature is fitted with a lorentzian convoluted with a gaussian. The linewidth of the lorentzian is

---

[1] The binding energy is measured with respect to the vacuum level.

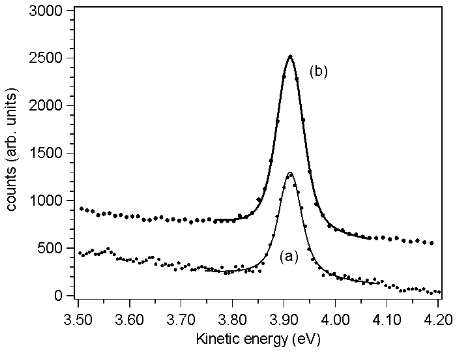

FIGURE A.1: Two-photon-photoemission spectra at a photon energy of 4.32 eV and at $k_{\|}$=0 collected with the high resolution (a) and the low resolution TOF (b). The feature at about 3.9 eV kinetic energy is ascribed to the n=1 image potential state. The lines represent the fit of the n=1 IPS with a lorentzian convoluted with a gaussian.

considered as a parameter in the fit, whereas the gaussian linewidth (σ), which accounts for instrumental resolution, has been estimated for both TOF spectrometers and kept fixed. The gaussian linewidth depends on the spectrometer resolution and the laser linewidth. The laser linewidth is the same for the two set of measurements: about 12 meV. The spectrometer resolution depends on the geometrical area of the multichannel plate and on the electronics temporal resolution. The estimated linewidth of the gaussian is about 45meV for the low resolution TOF and 35meV for the high resolution spectrometer. These values are confirmed by fitting the Fermi-edge measured with single photon photoemission at a photon energy of 6.28 eV on Ag(100) cooled at 160K. An isotropic emission of the photoelectrons is considered in the following. Once the gaussian linewidth is fixed, the intrinsic lorentzian linewidth is estimated by the fit.

In Fig. A.2, the behavior of the intrinsic linewidths against the parallel energy is showed for the two sets of experiments (a,c). The parallel energy is calculated using the following relations:

$$E_{\|} = \frac{\hbar^2 k_{\|}^2}{2m} \tag{A.1}$$

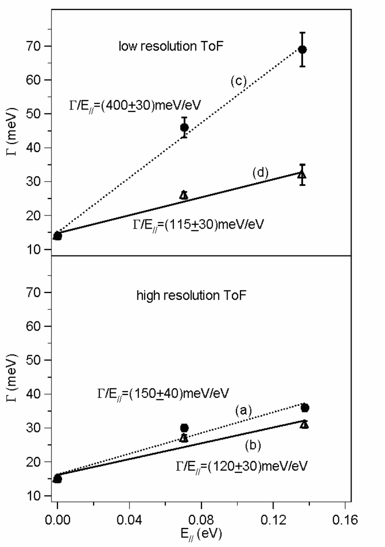

FIGURE A.2: The behavior of the intrinsic linewidth against the parallel energy is shown for the high and the low resolution TOF by fitting the IPS lineshape with a lorentzian convoluted with a gaussian ((a) and (c)) and with an integral of lorentzians convoluted with a gaussian ((b) and (d)). The lines represent the best linear fit of the experimental data (markers). The slopes are reported in the figure.

$$k_{\|} = \frac{\sqrt{2mE_{kin}}}{\hbar} \sin\theta \tag{A.2}$$

where E_{kin} is the photoelectron kinetic energy and θ is the angle between the perpendicular to the sample and the TOF. The intrinsic linewidth measured at $k_{\|}$=0 with the high resolution TOF (15±2 meV) is in agreement with that obtained with the low resolution TOF (14±2 meV). The inverse linewidth (47±7 fs), is in agrement with time-resolved measurements on Ag(100) previously reported in literature [22]. At $k_{\|}$=0.14 $\mathring{A}^{-1}$, which corresponds to an angle of 8°, the intrinsic linewidth measured with the high resolution TOF is about 20 meV smaller than the value measured with the low resolution TOF. The slope of the best linear fit of $E_{\|}$-dependent intrinsic linewidth obtained with the low

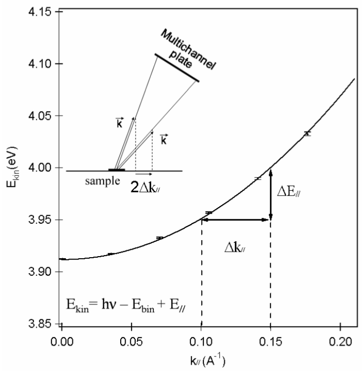

FIGURE A.3: In this figure the $k_{\|}$-spread related to the geometrical acceptance angle of the low resolution TOF detector is shown. At a specified angle, the detector collects photoelectrons with a different $k_{\|}$, therefore a sum of lorentzians each for a different $k_{\|}$ in the $k_{\|}$ range has to be considered in the fitting procedure. Due to the parabolic behavior of the kinetic energy versus $k_{\|}$, the $E_{\|}$-spread related to the $\Delta k_{\|}$ increases with $k_{\|}$. In the figure the experimental data (markers) are fitted with a parabolic curve (solid line), as discussed in Ref. [18].

resolution TOF is 400±0 meV/eV, whereas the slope with the high resolution TOF is about 150±40 meV/eV (Fig. A.2). The difference of linewidths of the two measurements (using high and low resolution TOF) can be ascribed to a spread in $k_{\|}$. The geometrical acceptance angle of the TOF implies that, at a specified angle, the TOF simultaneously collects photoelectrons with different $k_{\|}$-vector (see Fig. A.3).

In particular, for the low resolution TOF the maximum $\Delta k_{\|}$ spread is about 0.045 $\mathring{A}^{-1}$, whereas for the high resolution TOF $\Delta k_{\|}$ is about 0.015 $\mathring{A}^{-1}$. Therefore, each spectrum is expressed as a sum of lorentzians with different $k_{\|}$. Due to the parabolic $k_{\|}$ dispersion, each of these lorentzian correspond to a different kinetic energy value. To reconcile the intrinsic linewidth values measured with the two spectrometers, the IPS feature has to be fitted with a convolution of a gaussian with a sum of lorentzians. The sum of lorentzians can be expressed as:

$$f(E) = \frac{1}{E_2 - E_1} \int_{E_1}^{E_1} \frac{fwhm}{2} \frac{1}{(E - E_0)^2 + (\frac{fwhm}{2})^2} dE_0 \tag{A.3}$$

that gives

$$f(E) = \frac{1}{\pi(E_2 - E_1)} \left[-\arctan \frac{E - E_2}{\frac{fwhm}{2}} + \arctan \frac{E - E_1}{\frac{fwhm}{2}} \right] \tag{A.4}$$

where $fwhm$ is the full width at half maximum of the single $k_{\|}$-lorentzian, that is considered constant in the $k_{\|}$ range, E_0 is the energy position of the lorentzian, $E_1 = \hbar^2(k_{\|} - \Delta k_{\|})^2/2m$ and $E_2 = \hbar^2(k_{\|} + \Delta k_{\|})^2/2m$. Using this fitting procedure the intrinsic IPS linewidths at $k_{\|}$=0 are in agreement with the previous results, confirming that the $k_{\|}$-spread is not relevant at $k_{\|}$=0. The intrinsic linewidths at $k_{\|} \neq 0$ result the same, within the errors, for both high and low resolution TOF (Fig. A.2 (b,d)). The slope of the solid lines which represents the best linear fit of the IPS linewidths versus $E_{\|}$ is 120±30meV/eV and 115±30meV/eV for high and low resolution TOF, respectively. This slope is comparable with the slope obtained by the high resolution TOF using the single lorentzian fit (150±40meV/eV). Therefore, the contribution of the $k_{\|}$-spread in the IPS intrinsic linewidth measurement, can be neglected when the geometrical angular acceptance of the TOF implies a $k_{\|}$-spread of about 0.015 $\mathring{A}^{-1}$.

Appendix B

List of Acronyms and Frequently Used Notations

1D	One dimensional
2D	Two dimensional
3D	Three dimensional
2DEG	Two dimensional electron gas
2PPE	Two-photon photoemission
3PPE	Three-photon photoemission
a_0	Bohr radius
ARPES	Angle resolved photoemission spectroscopy
ATI	Above-threshold ionization
ATP	Above-threshold photoionization
BBO	Beta barium borate crystal
BE	Binding energy
BS	Beam splitter

CCD	Charge coupled device
Ch	Optical chopper
DOS	Density of states
$d_{\|\|}$-, π^*-bands	Energy bands resulting from the splitting of $3d$-bands in VO_2
$\Delta R/R$	Relative reflectivity variation
$\varepsilon(E)$	Complex dielectric function at energy E
E_{bin}	Binding energy
E_F	Fermi energy
E_{gap}	Energy gap
E_{kin}	Kinetic energy
$E_{\|\|}$	Energy relative to the momentum parallel to the sample surface
E_{vac}	Energy of the vacuum level
Φ	Work function
F	Filter
FD	Fermi-Dirac
$f(k)$	Electron distribution function as a function of k
FWHM	Full width half maximum
$\overline{\Gamma}$, $\overline{X}$, $\overline{M}$	Symmetry points of the surface Brillouin zone
Γ, L, U, X, W, K	Symmetry points of the bulk Brillouin zone
$G(\mathbf{k}, \omega)$	Electron Green function as a function of $\mathbf{k}$ and ω
$h\nu$	Photon energy
IMPT	Insulator-Metal phase transition
IPS	Image potential state
IR	Infrared
J_n	nth order Bessel function
k_F	Fermi momentum
$k_{\|\|}$	Momentum parallel to the sample surface
$k_\perp$	Momentum perpendicular to the sample surface

LEED	Low-energy electron diffraction
m	Electron rest mass
m^*	Electron effective mass
M	Mirror
M_1-phase	monoclinic phase
MP	Prism with an Al-coated side
n, k	Real and imaginary parts of the refraction index
n=0	Intrinsic surface state
n=1	First image potential state
n=2	Second image potential state
P	Polarizer
PH	Pin-hole
p polarization	Electric field parallel to the plane of incidence
Pr	Prism
R	Reflectivity
R-phase	Rutile phase
RPA	Random phase approximation
r_s	Seitz radius
$\Sigma^*(\mathbf{k},\omega)$	Irreducible self energy as a function of $\mathbf{k}$ and ω
SBZ	surface Brillouin zone
SM	Spherical mirror
s polarization	Electric field perpendicular to the plane of incidence
$T^{(n)}_{i\to f}$	nth order transition matrix element
T_c	Critical temperature
TOF	Time-of-flight
TOPG	Travelling-wave optical parametric generator
TR2PPE	Time-resolved two-photon photoemission
UHV	Ultra-high vacuum

UPS	Ultraviolet photoemission spectroscopy
XPS	X-ray photoemission spectroscopy
$W(\mathbf{k},\omega)$	Many-body potential as a function of $\mathbf{k}$ and ω

Bibliography

[1] U. Höfer, I. L. Shumay, C. Reuß, U. Thomann, W. Wallauer, and T. Fauster, Science **277**, 1480 (1997).

[2] N.-H. Ge, C. M. Wong, R. L. J. Lingle, J. D. McNeill, K. J. Gaffney, and C. B. Harris, Science **279**, 202 (1998).

[3] J. Kliewer, B. Berndt, E. V. Chulkov, V. M. Silkin, P. M. Echenique, and S. Crampin, Science **288**, 1399 (2000).

[4] P. M. Echenique, R. Berndt, E. V. Chulkov, T. Fauster, A. Goldmann, and U. Hofer, Surf. Sci. Reports **52**, 219 (2004).

[5] A. D. Miller, I. Bezel, K. J. Gaffney, S. Garrett-Roe, S. H. Liu, P. Szymanski, and C. B. Harris, Science **297**, 1163 (2002).

[6] W. Berthold, U. Höfer, P. Feulner, E. V. Chulkov, V. M. Silkin, and P. M. Echenique, Phys. Rev. Lett. **88**, 056805 (2002).

[7] A. Goldmann, V. Dose, and G. Borstel, Phys. Rev. B **32**, 1971 (1985).

[8] B. Reihl, K. H. Frank, and R. R. Schlitter, Phys. Rev. B **30**, 7328 (1984).

[9] Z. Li and S. Gao, Phys. Rev. B **50**, 15349 (1994).

[10] P. M. Echenique and J. B. Pendry, Progr. Surf. Sci. **32**, 111 (1990).

[11] P. M. Echenique and J. B. Pendry, J. Phys. C **11**, 2065 (1978).

[12] T. Fauster and W. Steinmann, in *Two-photon photoemission spectroscopy of image states*, Vol. 2 of *Electromagnetic Waves: Recent Development in Research*, edited by P. Halevi (Elsevier Science B. V., Amsterdam, 1995), Chap. 8, p. 347.

[13] K. Giesen, F. Hage, F. J. Himpsel, H. J. Riess, W. Steinmann, and N. V. Smith, Phys. Rev. B **35**, 975 (1987).

[14] J. Rundgren and G. Malström, Phys. Rev. Lett. **38**, 836 (1977).

[15] P. D. Johnson and N. V. Smith, Phys. Rev. B **27**, 2527 (1983).

[16] G. Binning, K. H. Frank, H. Fuchs, N. Garcia, B. Reihl, H. Roeher, F. Salvan, and A. R. Williams, Phys. Rev. Lett. **55**, 991 (1985).

[17] K. Giesen, F. Hage, F. J. Himpsel, H. J. Riess, and W. Steinmann, Phys. Rev. Lett. **55**, 300 (1985).

[18] G. Ferrini, C. Giannetti, D. Fausti, G. Galimberti, M. Peloi, G. Banfi, and F. Parmigiani, Phys. Rev. B **67**, 235407 (2003).

[19] K. Giesen, F. Hage, F. J. Himpsel, H. J. Riess, and W. Steinmann, Phys. Rev. B **35**, 971 (1987).

[20] G. Paolicelli *et al.*, Surf. Rev. and Lett. **9**, 541 (2002).

[21] R. W. Schoenlein, J. G. Fujimoto, G. L. Eesley, and T. W. Capehart, Phys. Rev. B **41**, 5436 (1990).

[22] I. L. Shumay, U. Höfer, C. Reuß, U. Thomann, W. Wallauer, and T. Fauster, Phys. Rev. B **58**, 13974 (1998).

[23] C. López-Bastidas, J. A. Maytorena, and A. Liebsch, Phys. Rev. B **65**, 035417 (2001).

[24] A. García-Lekue, J. M. Pitarke, E. V. Chulkov, A. Liebsch, and P. M. Echenique, Phys. Rev. Lett. **89**, 096401 (2002).

[25] E. V. Chulkov, V. M. Silkin, and P. M. Echenique, Surf. Sci. **391**, L1217 (1997).

[26] S. Schuppler, N. Fischer, T. Fauster, and W. Steinmann, Appl. Phys. A **51**, 322 (1990).

[27] P. M. Echenique, J. Osma, V. M. Silkin, E. V. Chulkov, and J. M. Pitarke, Appl. Phys. A **71**, 503 (2000).

[28] G. Farkas and C. Toth, Phys. Rev. A **41**, 4123 (1990).

[29] G. Petite, P. Agostini, R. Trainham, E. Mevel, and P. Martin, Phys. Rev. B **45**, 12210 (1992).

[30] G. Farkas, C. Toth, and A. Kohazikis, Opt. Eng. **32**, 2476 (1993).

[31] M. Aeschlimann, C. Schmuttenmaer, H. Elsayed-Ali, R. Miller, J. Cao, Y. Gao, and D. Mantell, J. Chem. Phys. **102**, 8606 (1995).

[32] G. Banfi, G. Ferrini, M. Peloi, and F. Parmigiani, Phys. Rev. B **67**, 035428 (2003).

[33] G. Ferrini, C. Giannetti, G. Galimberti, S. Pagliara, D. Fausti, F. Banfi, and F. Parmigiani, Phys. Rev. Lett. **92**, 2568021 (2004).

[34] A. Lugovskoy and I. Bray, Phys. Rev. B **60**, 3279 (1999).

[35] B. Rethfeld, A. Kaiser, M. Vicanek, and G. Simon, Phys. Rev. B **65**, 214303 (2002).

[36] D. Pines and P. Nozieres, *The Theory of Quantum Liquids* (Benjamin, New York, 1969).

[37] S. Anisimov, A. Bonch-Bruevich, M. El'yashevich, N. P. Y.A. Imas, and G. Romanov, **11**, 945 (1967).

[38] S. Anisimov, B. Kapeliovich, and T. Perel'man, **39**, 375 (1974).

[39] W. Fann, R. Storz, H. Tom, and J. Bokor, Phys. Rev. Lett. **68**, 2834 (1992).

[40] W. Fann, R. Storz, H. Tom, and J. Bokor, Phys. Rev. B **46**, 13592 (1992).

[41] D.Bejan and G.Raseev, Phys. Rev. B **55**, 4250 (1997).

[42] F. Banfi, C. Giannetti, G. Ferrini, G. Galimberti, S. Pagliara, D. Fausti, and F. Parmigiani, submitted to Phys. Rev. Lett.

[43] P. Petek and S. Ogawa, Progr. Surf. Sci. **56**, 239 (1997).

[44] N. Ashcroft and N. Mermin, *Solid State Physics* (Holt, Rinehart and Winston, New York, 1976).

[45] R. Groeneveld, R. Sprik, and A. Lagendijk, Phys. Rev. B **45**, 5079 (1992).

[46] C. Sun, F. Vallee, L. Acioli, E. Ippen, and J. Fujimoto, Phys. Rev. B **48**, 12365 (1993).

[47] R. Groeneveld, R. Sprik, and A. Lagendijk, Phys. Rev. B **51**, 11433 (1995).

[48] N. D. Fatti, R. Bouffanais, F. Vallee, and C. Flytzanis, Phys. Rev. Lett. **81**, 922 (1998).

[49] N. D. Fatti, C. Voisin, M. Achermann, S. Tzortzakis, D. Christofilos, and F. Vallee, Phys. Rev. B **61**, 16956 (2000).

[50] D. Lynch and W. Hunter, *Handbook of Optical Constants of Solids* (Academic Press, Orlando, 1985).

[51] S. Brorson, A. Kazeroonian, J. Moodera, D. Face, E. I. T.K. Cheng, M. Dresselhaus, and G. Dresselhaus, Phys. Rev. Lett. **64**, 2172 (1990).

[52] P. Agostini, F. Fabre, G. Mainfray, and G. Petite, Phys. Rev. Lett. **42**, 1127 (1979).

[53] T. J. McIlrath, P. H. Bucksbaum, R. R. Freeman, and M. Bashkansky, Phys. Rev. A **35**, 4611 (1987).

[54] R. Freeman, P. Bucksbaum, H. Milchberg, S. D. D. Schumacher, and M. Geusic, Phys. Rev. Lett. **59**, 1092 (1987).

[55] G. D. Gillen and L. D. V. Woerkom, Phys. Rev. A **68**, 033401 (2003).

[56] M. J. Dewitt and R. Levis, Phys. Rev. Lett. **81**, 5101 (1998).

[57] S. Luan, R. Hippler, H. Schwier, and H. O. Lutz, **9**, 489 (1989).

[58] W. S. Fann, R. Storz, and J. Bokor, Phys. Rev. B **44**, 10980 (1991).

[59] F. H. M. Faisal, *Theory of Multiphoton Processes* (Plenum, New York, 1987).

[60] L. Hedin, Phys. Rev. **139**, A796 (1965).

[61] H. Ehrenreich and H. R. Phillip, Phys. Rev. **128**, 1622 (1962).

[62] R. W. Schoenlein, J. G. Fujimoto, G. L. Eesley, and T. W. Capehart, Phys. Rev. Lett. **61**, 2596 (1988).

[63] M. Wolf, A. Hotzel, E. Knoesel, and D. Velic, Phys. Rev. B **59**, 5926 (1999).

[64] G. Farkas, C. Toth, S. D. Moustaizis, N. A. Papadogiannis, and C. Fotakis, Phys. Rev. A **46**, 3605 (1992).

[65] D. Volkov, Z. Phys. **456**, 250 (1935).

[66] J. Seely and E. Harris, Phys. Rev. A **7**, 1064 (1973).

[67] A. Krakovsky and J. K. Percus, Phys. Rev. B **53**, 7352 (1996).

[68] S. Doniach and E. Sondheimer, *Grren's Functions for Solid State Physicists* (W.A. Benjamin, New York, 1974).

[69] M. Gell-Mann and K. Brueckner, Phys. Rev. **106**, 364 (1957).

[70] D. DuBois, Ann. Phys. **7**, 174 (1959).

[71] A. Isihara and T. Toyoda, Phys. Rev. B **21**, 3358 (1980).

[72] P. Echenique, J. Pitarke, E. Chulkov, and A. Rubio, Chem. Phys. **251**, 1 (2000).

[73] C. Rischel, A. Rousse, I. Uschmann, P. Albouy, J. Geindre, P. Audebert, J. Gauthier, and E. F .

[74] C. Siders *et al.*, Science **286**, 1340 (1999).

[75] K. Sokolowski-Tinten, C. Blome, J. Blums, A. Cavalleri, C. Dietrich, A. Tarasevitch, I. Uschmann, and E. F .

[76] M. Becker, A. Buckman, R. Walser, T. Lépine, P. Georges, and A. Brun, Appl. Phys. Lett. **65**, 1507 (1994).

[77] A. Cavalleri, C. Tóth, C. Siders, J. Squier, F. Ráksi, P. Forget, and J. Kieffer, Phys. Rev. Lett. **87**, 2374011 (2001).

[78] E. Collet *et al.*, Science **300**, 612 (2003).

[79] F. Morin, Phys. Rev. Lett. **3**, 34 (1959).

[80] M. Marezio, D. McWhan, J. Remeika, and P. Dernier, Phys. Rev. B **5**, 2541 (1972).

[81] A. Zylbersztejn and N. Mott, Phys. Rev. B **11**, 4383 (1975).

[82] D. Paquet and P. Leroux-Hugon, Phys. Rev. B **22**, 5284 (1980).

[83] S. Shin *et al.*, Phys. Rev. B **41**, 4993 (1990).

[84] T. Rice, H. Launois, and J. Poiget, Phys. Rev. Lett. **73**, 3042 (1994).

[85] P. Allen, H. Berger, O. Chauvet, L. Forro, T. Jarlborg, A.Junod, B. Revaz, and G. Santi, Phys. Rev. B **53**, 4393 (1996).

[86] K. Okazaki, H. Wadati, A. Fujimori, M. Onoda, Y. Muraoka, and Z. Hiroi, Phys. Rev. B **69**, 1651041 (2004).

[87] D. Alder and H. Brooks, Phys. Rev. **155**, 826 (1967).

[88] J. Goodenough, J. Solid State Chem. **3**, 490 (1961).

[89] M. Gupta, A. Freeman, and D. Ellis, Phys. Rev. B **16**, 3338 (1977).

[90] R. Wentzcovitch, W. Schulz, and P. Allen, Phys. Rev. Lett. **72**, 3389 (1994).

[91] A. Cavalleri, H. Chong, S. Fourmaux, T. Glover, P. Heimann, J. Kieffer, B. Mun, H. Padmore, and R. Schoenlein, Phys. Rev. B **69**, 153106 (2004).

[92] M. Imada, A. Fujimori, and Y. Tokura, Rev. Mod. Phys. **70**, 1039 (1998).

[93] V. Eyert, Ann. Phys. **11**, 1 (2002).

[94] H. Verleur, J. A.S. Barker, and C. Berglund, Phys. Rev. **172**, 788 (1968).

[95] M. Abbate, F. de Groot, J. Fuggle, Y. Ma, C. Chen, F.Sette, A. Fujimori, Y. Ueda, and K. Kosuge, Phys. Rev. B **43**, 7263 (1991).

[96] A. Cavalleri and Th. Dekorsy and H.H. Chong and J.C. Kieffer and R.W. Schoenlein, Cond. Mat. 0403214.

[97] H. Zeiger, J. Vidal, T. Cheng, E. Ippen, G. Dresselhaus, and M. Dresselhaus, Phys. Rev. B **45**, 768 (1992).

[98] A summary of the optical properties of Si and Si_3N_4 as a function of the light wavelenght is available on the website: http://www.luxpop.com/.
The data reported have been taken from:
A.B. Djurisic and E.H. Li, Appl. Opt. **37**, 5291 (1998).
S. Adachi, Phys. Rev. B **38**, 12966 (1988).
J. Humlicek, M. Garriga, M.I. Alonso and M. Cardona, J. Appl. Phys. **65**, 2827 (1989).

List of publications

· **Effective mass and momentum-resolved intrinsic linewidth of image-potential states on Ag(100)**
G. Ferrini, C. Giannetti, D. Fausti, G. Galimberti, M. Peloi, G.P. Banfi and F. Parmigiani, *Phys. Rev. B* **67**, 235407 (2003).

· **Violation of the Electric-Dipole Selection Rules in Indirect Multiphoton Excitation of Image- Potential States on Ag(100)**
G. Ferrini, C. Giannetti, G. Galimberti, S. Pagliara, D. Fausti, F. Banfi and F. Parmigiani, *Phys. Rev. Lett.* **92**, 2568021 (2004).

· **Measurements of intrinsic linewidth versus parallel momentum of image-potential states on Ag(100)**
C. Giannetti, G. Galimberti, S. Pagliara, G. Ferrini, F. Banfi, D. Fausti and F. Parmigiani, *Surf. Sci.* **566-568**, 502 (2004).

· **Experimental evidence of above-threshold photoemission in solids**
F. Banfi, C. Giannetti, G. Ferrini, G. Galimberti, S. Pagliara , D. Fausti, and F. Parmigiani, *Phys. Rev. Lett.* **94**, 037601 (2005).

· **Athermal electron distribution probed by femtosecond multiphoton photoemission from image potential states**
G. Ferrini, C. Giannetti, S. Pagliara, F. Banfi, G. Galimberti and F. Parmigiani, in press on *J. Electr. Spectrosc. Relat. Phenom.*

· **Excitation and photoemission dynamics of photo-induced non-equilibrium electron gas in metals**
C. Giannetti, S. Pagliara, G. Ferrini, G. Galimberti, F. Banfi, and F. Parmigiani, submitted to *Phys. Rev. B.*

· **Monte Carlo transverse emittance study on Cs_2Te**
F. Banfi, E. Pedersoli, S. Pagliara, C. Giannetti, G. Ferrini, G. Galimberti, B. Ressel, and F. Parmigiani, *in preparation.*

· **Quantum Yield measurements of femtosecond vectorial photoemission on Cu photocathodes**
E. Pedersoli, F. Banfi, S. Pagliara, G. Galimberti, G. Ferrini, C. Giannetti, and F. Parmigiani, *in preparation.*

Acknowledgements

I conclude this thesis with a few acknowledgements. First of all I want to thank Prof. Fulvio Parmigiani, my scientific supervisor and guide, who made this work possible. I thank all the people working at the Elphos project, during three demanding and satisfactory years: (in alphabetical order) Francesco Banfi, Gabriele Ferrini, Gianluca Galimberti and Stefania Pagliara. I acknowledge also Daniele Fausti, Emanuele Pedersoli and Marco Peloi, who spent in Brescia a smaller (but intense) period. I want to acknowledge Andrea Cavalleri (LBNL, Berkeley) for supplying us the VO_2 samples and for the useful discussions. I thank Prof. Enrico Zaglio and Maurizio Bertoni for the qualified technical support and all the people who helped me, with discussions or suggestings, during this work: Barbara Ressel (Elettra, Trieste), Luca Gavioli and Fausto Borgonovi (Università Cattolica del Sacro Cuore), Luca Molinari (Università degli Studi di Milano). Finally I acknowledge Prof. R. Bonifacio, the director of the Ph. D. degree course at the ”Università degli Studi” of Milan.

Adesso alcuni ringraziamenti in italiano, lingua in cui mi risulta più facile esprimere gratitudine per il tempo, la fatica e le soddisfazioni affrontate insieme.

Grazie a Fulvio Parmigiani, che, tre anni fa, ha creduto in me anche senza conoscermi (e poi il culatello e la torta fritta!). Grazie a Gabriele Ferrini per la sua pazienza in ogni situazione (anche se fa riscrivere gli articoli troppe volte). Grazie a PierGianluca Galimberti, perchè non se la prende mai, ma è sempre un bell'esempio, anche in cose più importanti della fisica. Grazie a Stefania Pagliara e a Luigi Sangaletti, soprattutto per aver condiviso per lungo tempo la prova più difficile: i disagi delle ferrovie italiane. Grazie a Marco Peloi per l'eredità lasciata e per il Trombettin. Un ringraziamento particolare a Francesco Banfi, per aver condiviso in maniera coerente l'ufficio e un tratto importante di strada. Un shumë faleminderit alla ”mente” Daniele Fausti, per tanti motivi.

Un ringraziamento ad Andrea Zanzani, segretario del corso di dottorato, perchè rendere la vita più facile alle persone non è cosa da poco.

Infine vorrei ringraziare tutta la mia famiglia, che mi ha messo in condizione di poter lavorare a ritmi faticosi per questi tre anni. Un ultimo ringraziamento a Elena e a tutti gli amici: si cresce, si cambia, ma non ci si divide.